Stress, strain and dissipation accurate 3-field formulation for inelastic isochoric deformation

M. Chiumenti, M. Cervera, C.A. Moreira and G.B. Barbat
International Center for Numerical Methods in Engineering (CIMNE)
Universidad Politécnica de Cataluña (UPC)
Edificio C1, Campus Norte, Gran Capitán s/n, 08034 Barcelona Spain.
e-mail: michele@cimne.upc.edu, web page: http://www.cimne.com

KEYWORDS: Stress accurate, incompressible limit, Mixed three-field finite element technology, Variational Multi Scale (VMS) stabilization.

Abstract

This work exploits the high accuracy of the mixed $\mathbf{u}/\mathbf{e}/p$ 3−field formulation to address materially non-linear inelastic problems including isochoric deformations.

Motivated by the strain-driven format of several constitutive equations used in FEA, the mixed $\mathbf{u}/\mathbf{s}/p$ formulation is reinterpreted, selecting the deviatoric strains as primary variables, together with the displacements and the pressure field.

The mixed formulation is complemented with several constitutive equations suitable for Solid and Fluid Mechanics.

The convergence rate upon mesh refinement, as well as the enhanced accuracy of the stress and strain fields is proven in several non-linear problems with isochoric deformation in both the elastic and the inelastic ranges. $2D$ and $3D$ problems involving different FE discretizations are solved with $J2-$plasticity, $J2-$damage and Bingham models, all of them including strain localization. Numerical results show that perfectly convergent and mesh-independent results are achieved in terms of peak load, failure mechanism, stress release and energy dissipation. Revealing comparison with the $\mathbf{u}/p$ formulation is also addressed.

1 Introduction

The aim of this work is to exploit the advantages of the mixed displacement/deviatoric-strain/ pressure ($\mathbf{u}/\mathbf{e}/p$) 3−field formulation for the solution of material non-linear problems in Computational Solids and Fluid Mechanics. The authors have introduced this FE technology in a previous work where enhanced accuracy was proven for both compressible and incompressible elasticity problems [28]. The scope of this work is to solve materially non-linear Stokes problems where a variety of constitutive laws can be adopted for solid and fluid analyses. Within the former setting, elasticity, plasticity or damage constitutive laws are tackled within the infinitesimal strain theory, while the latter is suitable to analyze different rigid-viscoplastic flows such as Bingham, Norton-Hoff, Sheppard-Wright and Carreau, among others.

This flexibility is very appealing to address the numerical simulation of different industrial manufacturing processes including metal forming, forging, extrusion, Friction Stir Welding (FSW), or machining operations, and many others. All these processes are non-linear, present stress concentrations and most of them show strain localization through the formation of shear bands. Moreover, the deviatoric nature of the plastic strains arising from the plasticity models used in metal forming, as well as the intrinsic isochoric nature of the constitutive laws used to characterize the rigid-plastic material flow, require a FE technology able to deal with the incompressibility constraint. Hence, stress accuracy and performance in the incompressible limit are both mandatory requirements that motivate this work.

Popular solutions to tackle the quasi-incompressible limit are: the reduced and selective integration methods ([42], [45], [43], [51]), the B-bar and F-bar elements ([33], [68], [34], [58]) and the enhanced assumed strain methods ([66], [32], [47]). Although they cannot be used in the incompressible limit, these approaches have proven to be reliable in quasi-isochoric problems for hexahedral elements but they do not have a straightforward generalization to tetrahedral grids, being the preferred choice for the automatic mesh generation.

Alternatively, the use of mixed displacement/pressure ($\mathbf{u}/p$) or velocity/pressure ($\mathbf{v}/p$) formulations have been proposed to avoid the volumetric locking when approaching the incompressible limit. The use of different stabilization techniques and particularly the Variational Multi-Scale (VMS) method allows for the adoption of equal-order piecewise linear interpolations for both displacement (velocity) and pressure, circumventing the *inf-sup* conditions ([2], [12]) for the Stokes and Navier-Stokes problems ([46], [38], [29]). The approach was extended to incompressible elasticity ([44], [39]), elastoplasticity ([53], [55]), elasto-dynamic problems ([63], [64], [61], [50] and [69]) and hyperelastic finite deformation ([54], [56], [62] and [11]). The Orthogonal Subgrid Scales (OSS) method ([29]) was presented by the authors to address problems in incompressible elasticity and J2-plasticity, and damage analysis including the strain localization process induced by strain-softening laws ([26], [15], [27], [1], [16], [17] and [19]).

The stress/strain accuracy can be enhanced by adopting the mixed displacement/stress ($\mathbf{u}/\boldsymbol{\sigma}$) formulation, where both displacements and stresses are used as primary variables in the finite element discretization ([10], [9], [60], [35], [36], [20]). This given, a natural way to access the incompressible limit with stress accuracy consists of splitting the stress tensor into its deviatoric and spherical (volumetric) parts, being the latter the pressure field, p. Hence, when the (deviatoric)-stress tensor, $\mathbf{s}$, together with both the pressure and the displacement fields are taken as primary variables, the mixed 3−field ($\mathbf{u}/\mathbf{s}/p$) formulation arises, as shown in [28].

Nevertheless, numerous material laws and the corresponding computational algorithms are strain-driven: the strain tensor is the input to the constitutive equations while the stress tensor is the corresponding outcome. This motivates the mixed displacement/strain ($\mathbf{u}/\boldsymbol{\varepsilon}$) formulation. Thus, the same implementation of the constitutive laws used for the standard irreductible (displacements-based) element is suitable for the mixed $\mathbf{u}/\boldsymbol{\varepsilon}$ technology.

The displacement/strain formulation was successfully used to encompass non-linear problems including finite displacements in dynamic problems [48], strain-localization in plasticity ([6], [23], [49] and [24]) and crack propagation using damage models in mode-I ([20], [21] and [22]) and mixed modes ([7], [8] and [25]). However, the strain/displacement formulation is not able to reach the incompressible limit. This is the motivation of the present work: the development of a mixed displacement/(deviatoric)-strains/pressure ($\mathbf{u}/\mathbf{e}/p$) 3−field formulation as accurate as the strain/displacement FE technology but able to treat isochoric deformations.

The outline of the paper is as follows. In Section 2 and Section 3, the framework suitable for solids and fluids is presented. The continuum problem (strong form) is shown in Sections 2.1 and 3.1, respectively. The volumetric/deviatoric split of the stresses and strains as well as the constitutive tensor is described in Section 2.2. Next, the constitutive equations suitable for both computational solid (Section 2.3) and fluid mechanics (Section 3.2) are described. The weak form of the 3−field formulation is detailed in Sections 2.4 and 3.3, respectively. Sections 2.5 and 3.4 deal with the discrete approximation of the problem by the Galerkin method. The Variational Multi-Scale (VMS) approach required when using equal order linear interpolation for all fields is described in Section 2.6. This method allows for circumventing the inf-sup stability condition [12]. Section 4 shows different numerical examples to assess the accuracy and robustness of the proposed formulation.

2 Solid mechanics

2.1 The continuum problem

Let us denote by $\Omega(\mathbf{X}) \in \mathbb{R}^{n_{\text{dim}}}$ an open and bounded *material* domain of n_{dim} dimensions where $\mathbf{X}$ are the coordinates of its *material* points. The boundary $\partial\Omega$ is split into $\partial\Omega_u$ and $\partial\Omega_t$, being $\partial\Omega = \partial\Omega_u \cup \partial\Omega_t$ and $\partial\Omega_u \cap \partial\Omega_t = 0$, such that the prescribed displacements, $\overline{\mathbf{u}}$, are specified on $\partial\Omega_u$ (Dirichlet boundary conditions) and the prescribed tractions, $\overline{\mathbf{t}}$, are applied on $\partial\Omega_t$ (Neumann boundary conditions).

The continuum mechanical problem is defined by the following 3 equations:

$$\nabla \cdot \boldsymbol{\sigma} + \mathbf{b} = \mathbf{0} \tag{1}$$

$$\boldsymbol{\sigma} - \mathbb{C} : \boldsymbol{\varepsilon} = \mathbf{0} \tag{2}$$

$$\boldsymbol{\varepsilon} - \nabla^s \mathbf{u} = \mathbf{0} \tag{3}$$

where the unknowns are the displacement $\mathbf{u}(\mathbf{X})$, the Cauchy stress $\boldsymbol{\sigma}(\mathbf{X})$ and the strain fields $\boldsymbol{\varepsilon}(\mathbf{X})$, respectively. The first one is the *balance of momentum (equilibrium) equation*, the second is the *constitutive equation* and the last one is the *kinematic equation* (in the hypothesis of infinitesimal strains), and where $\mathbf{b}$ are the external loads per unit of volume and $\mathbb{C}$ is a generic 4^{th} order (secant) constitutive tensor.

Replacing the strains from Eq. (3) into the constitutive Eq. (2) and substituting the resulting stresses into Eq. (1), the result is *Navier*'s equation:

$$\nabla \cdot (\mathbb{C} : \nabla^s \mathbf{u}) + \mathbf{b} = \mathbf{0} \tag{4}$$

which is written in terms of the displacement field only, being the strains and the stresses:

$$\boldsymbol{\varepsilon}(\mathbf{u}) = \nabla^s \mathbf{u} \tag{5}$$

$$\boldsymbol{\sigma}(\mathbf{u}) = \mathbb{C} : \boldsymbol{\varepsilon}(\mathbf{u}) \tag{6}$$

Alternatively, the mixed $\boldsymbol{\sigma}/\mathbf{u}$ formulation uses both stresses and displacements as master fields:

$$\nabla \cdot \boldsymbol{\sigma} + \mathbf{b} = \mathbf{0} \tag{7}$$

$$\boldsymbol{\sigma} - \mathbb{C} : \nabla^s \mathbf{u} = \mathbf{0} \tag{8}$$

obtained by substituting Eq.(3) into Eq.(2).

Nevertheless, the constitutive equations, as used in FEM, are generally strain-driven, hence it is convenient to keep the strains as one of the independent variables, together with the displacement field, as:

$$\nabla \cdot (\mathbb{C} : \boldsymbol{\varepsilon}) + \mathbf{b} = \mathbf{0} \tag{9}$$

$$\boldsymbol{\varepsilon} - \nabla^s \mathbf{u} = \mathbf{0} \tag{10}$$

The result is the mixed $\boldsymbol{\varepsilon}/\mathbf{u}$ formulation, where the constitutive Eq. (2) has been plugged into the balance Eq. (1) while Eq. (10) enforces the kinematic constraint.

2.2 The volumetric/deviatoric split

Most of the constitutive equations can be split into their volumetric and deviatoric components by assuming a volumetric/deviatoric split of the free energy potential. This split implies that: (i) the volumetric deformation (volume change) is governed by the pressure field, only; (ii) the distortions are induced by the deviatoric part of the stress field. Hence, the two deformation modes are uncoupled.

Let us define the rank−4 volumetric and deviatoric projection tensors, $\mathbb{V}$ and $\mathbb{P}$, as follows:

$$\mathbb{V} = \frac{1}{3}(\mathbf{I} \otimes \mathbf{I}) \tag{11}$$

$$\mathbb{P} = \mathbb{I} - \frac{1}{3}(\mathbf{I} \otimes \mathbf{I}) \tag{12}$$

$$\mathbb{P} + \mathbb{V} = \mathbb{I} \tag{13}$$

where $\mathbb{I} = [\delta_{ij}\delta_{kl}]$ and $\mathbf{I} = [\delta_{ij}]$ are the rank−4 and the rank−2 identity tensors, respectively (δ_{ij} is Kronecker's delta).

The spherical (volumetric) and the deviatoric parts of the stress tensor, $\boldsymbol{\sigma}$, are obtained as:

$$\mathbb{V} : \boldsymbol{\sigma} = \frac{1}{3}(\mathbf{I} \otimes \mathbf{I}) : \boldsymbol{\sigma} = p\,\mathbf{I} \tag{14}$$

$$\mathbb{P} : \boldsymbol{\sigma} = \left[\mathbb{I} - \frac{1}{3}(\mathbf{I} \otimes \mathbf{I})\right] : \boldsymbol{\sigma} = \boldsymbol{\sigma} - p\,\mathbf{I} = \mathbf{s} \tag{15}$$

where $p(\boldsymbol{\sigma}) = \frac{1}{3}(\boldsymbol{\sigma} : \mathbf{I}) = \frac{1}{3}\text{tr}(\boldsymbol{\sigma})$ is the *pressure* and $\mathbf{s} = \text{dev}(\boldsymbol{\sigma})$ are the deviatoric stresses. This given, the stress tensor can be rebuilt adding both components of the split as:

$$\boldsymbol{\sigma} = p\,\mathbf{I} + \mathbf{s} \tag{16}$$

The same procedure is used to split the strain tensor $\boldsymbol{\varepsilon}$, as:

$$\mathbb{V} : \boldsymbol{\varepsilon} = \frac{1}{3}(\mathbf{I} \otimes \mathbf{I}) : \boldsymbol{\varepsilon} = \frac{1}{3} e_{vol}\,\mathbf{I} \tag{17}$$

$$\mathbb{P} : \boldsymbol{\varepsilon} = \left[\mathbb{I} - \frac{1}{3}(\mathbf{I} \otimes \mathbf{I})\right] : \boldsymbol{\varepsilon} = \boldsymbol{\varepsilon} - \frac{1}{3} e_{vol}\,\mathbf{I} = \mathbf{e} \tag{18}$$

where $e_{vol} = \boldsymbol{\varepsilon} : \mathbf{I} = \text{tr}(\boldsymbol{\varepsilon})$ and $\mathbf{e} = \mathbb{P} : \boldsymbol{\varepsilon} = \text{dev}(\boldsymbol{\varepsilon})$ are the volumetric and deviatoric component of $\boldsymbol{\varepsilon}$, respectively. This tensor is rebuilt as:

$$\boldsymbol{\varepsilon} = \frac{1}{3}\, e_{vol}\,\mathbf{I} + \mathbf{e} \tag{19}$$

In solid mechanics, the constitutive relationship between stresses and strains is expressed in secant form as:

$$\boldsymbol{\sigma} = \mathbb{C} : \boldsymbol{\varepsilon} \tag{20}$$

where the constitutive tensor $\mathbb{C}$ is split as:

$$\mathbb{C} = \mathbb{C}^{vol} + \mathbb{C}^{dev} \tag{21}$$

$\mathbb{C}^{vol}$ and $\mathbb{C}^{dev}$ being the *spheric* and the *deviatoric* parts of the tensor, extracted as:

$$\mathbb{C}^{vol} = \mathbb{V} : \mathbb{C} \tag{22}$$

$$\mathbb{C}^{dev} = \mathbb{P} : \mathbb{C} \tag{23}$$

Introducing the split of stresses and strains given by Eqs. (16) and (19) into Eq. (20), the constitutive relationship can be rewritten as:

$$p\,\mathbf{I} + \mathbf{s} = \mathbb{C} : \left(\frac{1}{3} e_{vol}\,\mathbf{I} + \mathbf{e}\right) \tag{24}$$

that is:

$$p = C^{vol}\, e_{vol} \tag{25}$$

$$\mathbf{s} = \mathbb{C}^{dev} : \mathbf{e} \tag{26}$$

which are the volumetric and the deviatoric components of the original constitutive equation (20), being $C^{vol} = \frac{1}{9}\mathbf{I} : \mathbb{C} : \mathbf{I}$.

Note that in case of *isotropic* materials the constitutive tensor can be written as:

$$\mathbb{C}^{vol} = 3\bar{K}\,\mathbb{V} = \bar{K}\,(\mathbf{I} \otimes \mathbf{I}) \tag{27}$$

$$\mathbb{C}^{dev} = 2\bar{G}\,\mathbb{P} = 2\bar{G}\,\left[\mathbb{I} - \frac{1}{3}(\mathbf{I} \otimes \mathbf{I})\right] \tag{28}$$

where $\bar{K}$ and $\bar{G}$ are the effective *bulk modulus* and the effective *shear modulus* of the material, respectively. Thus, the constitutive equation reduces to:

$$p = \bar{K}\ e_{vol} \tag{29}$$
$$\mathbf{s} = 2\bar{G}\ \mathbf{e} \tag{30}$$

When approaching the incompressible limit, $\bar{K} \to \infty$, it is convenient to write Eq. (29) as:

$$e_{vol} = \frac{p}{\bar{K}} \tag{31}$$

so that, in the limit, Eq. (31) transforms into: $e_{vol} = 0$, or , making use of Eq. (3), as the kinematic constraint:

$$\nabla \cdot \mathbf{u} = 0 \tag{32}$$

Remark 1 *The effective values of $\bar{K}$ and $\bar{G}$ depend on the actual constitutive equations used to characterize the material behavior, as illustrated in the following Section. For isotropic elasticity, these parameters correspond to their elastic counterparts: $\bar{K} = K$ and $\bar{G} = G$.*

2.3 Constitutive modeling

Firstly, the elastic constitutive equation is derived from the strain energy density function (hyper-elastic model). Next and following the same procedure, both $J2$-plasticity and $J2$-damage models are detailed including the evolution laws of the corresponding internal variables and the definition of the mechanical dissipation. The latter is used to show the accuracy of the 3-field formulation.

2.3.1 Elasticity

Elasticity is the starting point to introduce the volumetric/deviatoric split as well as the basis for the following elasto-plastic or elasto-damage constitutive models. In particular, *incompressible* elasticity is widely used in different applications such as rubbers, elastomers, biological tissues, etc.

Let us write the strain energy density function, Ψ, as:

$$\Psi = \tfrac{1}{2}\ \boldsymbol{\varepsilon} : \mathbb{C} : \boldsymbol{\varepsilon} \tag{33}$$

and introducing the split of the strain tensor in Eq. (19), it can be split as:

$$\Psi = \Psi_{vol}\left(e_{vol}\right) + \Psi_{dev}\left(\mathbf{e}\right) = \tfrac{1}{2}\ K\ e_{vol}^2 + \tfrac{1}{2}\ 2G\ \mathbf{e} : \mathbf{e} \tag{34}$$

where the bulk modulus $K = \frac{E}{3(1-2\nu)}$ and the shear modulus $G = \frac{E}{2(1+\nu)}$ are defined in terms of Young's modulus and Poisson's ratio, E and ν, respectively.

Applying Coleman's method [31], the rate of mechanical dissipation, $\dot{D}_{mech}$, is defined as:

$$\dot{D}_{mech} = \boldsymbol{\sigma} : \dot{\boldsymbol{\varepsilon}} - \dot{\Psi} \geq 0 \tag{35}$$

and using the split of the stress tensor in Eq. (16), the mechanical dissipation results in:

$$\dot{D}_{mech} = \left(p - \frac{\partial \Psi}{\partial e_{vol}}\right)\ \dot{e}_{vol} + \left(\mathbf{s} - \frac{\partial \Psi}{\partial \mathbf{e}}\right) : \dot{\mathbf{e}} \geq 0 \tag{36}$$

From this, the constitutive equations of the hyperelastic problem are derived as:

$$p = \frac{\partial \Psi}{\partial e_{vol}} = K\ e_{vol} \tag{37}$$

$$\mathbf{s} = \frac{\partial \Psi}{\partial \mathbf{e}} = 2G\ \mathbf{e} \tag{38}$$

and the mechanical dissipation cancels out:

$$\dot{D}_{mech} = 0 \tag{39}$$

2.3.2 $J2-$plasticity

The main hypothesis of the $J2$-*elasto-plastic constitutive model* consists of the additive split of the total deviatoric strains, $\mathbf{e}$, into their elastic and plastic counterparts, $\mathbf{e}^e$ and $\mathbf{e}^p$, respectively, as:

$$\mathbf{e} = \mathbf{e}^e + \mathbf{e}^p \tag{40}$$

Hence, the (elastic) strain energy density function, Ψ^e, is written in terms of the (total) volumetric deformation and the elastic deviatoric strains:

$$\Psi^e = \Psi^e_{vol}\left(e_{vol}\right) + \Psi^e_{dev}\left(\mathbf{e}^e\right) \tag{41}$$

$$= \tfrac{1}{2}\ K\ e^2_{vol} + \tfrac{1}{2}\ 2G\ \mathbf{e}^e : \mathbf{e}^e \tag{42}$$

$$= \tfrac{1}{2}\ K\ e^2_{vol} + \tfrac{1}{2}\ 2G\ \ (\mathbf{e} - \mathbf{e}^p) : (\mathbf{e} - \mathbf{e}^p) \tag{43}$$

Applying Coleman's method [31]:

$$\dot{D}_{mech} = \left(p - \frac{\partial \Psi^e}{\partial e_{vol}}\right)\ \dot{e}_{vol} + \left(\mathbf{s} - \frac{\partial \Psi^e}{\partial \mathbf{e}^e}\right) : \dot{\mathbf{e}}^e + \mathbf{s} : \dot{\mathbf{e}}^p \geq 0 \tag{44}$$

the constitutive equations of the $J2$-*elasto-plastic constitutive model* are:

$$p = K\ e_{vol} \tag{45}$$

$$\mathbf{s} = 2G\ \mathbf{e}^e = 2G\ \ (\mathbf{e} - \mathbf{e}^p) \tag{46}$$

while the mechanical dissipation results in:

$$\dot{D}_{mech} = \mathbf{s} : \dot{\mathbf{e}}^p \geq 0 \tag{47}$$

The evolution of the plastic deformations, $\mathbf{e}^p$, depends on the definition of the yield surface. The von Mises yield function, ϕ, typically used in isotropic $J2$-plasticity, is defined as:

$$\phi = s_{eq} - \sigma_y \leqslant 0 \tag{48}$$

where $s_{eq} = \sqrt{\frac{3}{2}}\ \|\mathbf{s}\| = \sqrt{3}\sqrt{J2}$ is the *equivalent* von Mises stress, being $J2$ the 2^{nd} invariant of the deviatoric stress tensor. The tensile strength of the material is defined as:

$$\sigma_y = \sigma_{yo} - q\left(\xi\right) \tag{49}$$

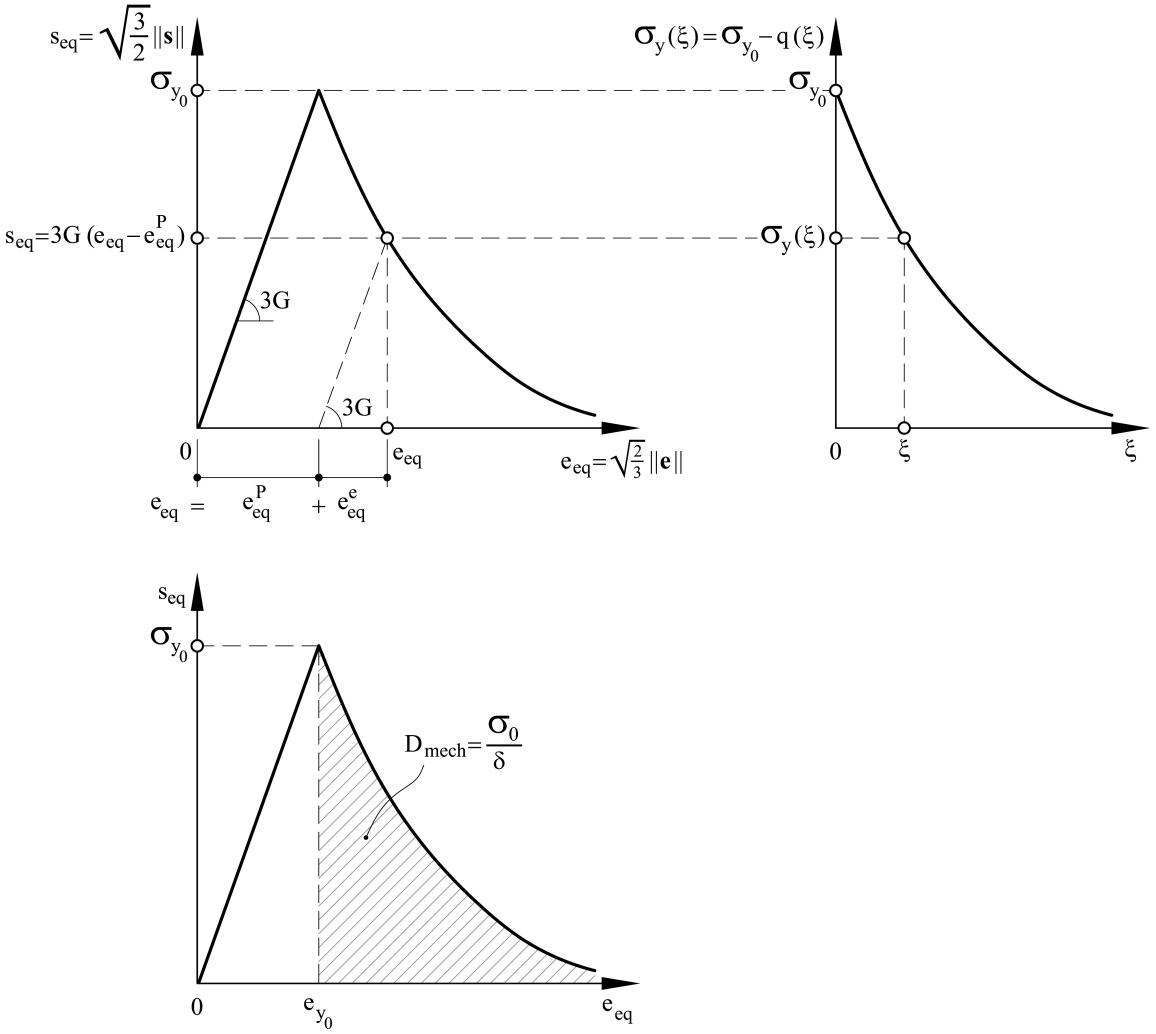

Figure 1: J2 Elasto-plastic model.

where σ_{yo} is the initial yield stress and $q(\xi)$ is the stress-like internal variable, conjugate to the *isotropic hardening/softening* variable ξ, and defined as:

$$q(\xi) = -(\sigma_\infty - \sigma_{yo})\,[1 - \exp(-\delta\xi)] \tag{50}$$

where σ_∞ is the saturation (ultimate) stress and δ is the coefficient of the saturation hardening/softening law (see Figure 1).

Remark 2 *The von Mises yield function can be defined by the equivalent format as:*

$$\phi^* = \|\mathbf{s}\| - R \leqslant 0 \tag{51}$$

where $R = \sqrt{\frac{2}{3}}\sigma_y(\xi)$ *is the radius of the cylinder that characterizes the von Mises yield surface [65].*

Let us introduce the rate of plastic work $\dot{W}^p(\mathbf{s},q)$, defined as:

$$\dot{W}^p(\mathbf{s},q) = \mathbf{s} : \dot{\mathbf{e}}^p + q\ \dot{\xi} \tag{52}$$

The evolution laws of both the plastic strains and the isotropic hardening/softening variable are obtained through the principle of maximum (plastic) work [65]. Thus, the functional:

$$\mathcal{F}(\mathbf{s},q) = -\dot{W}^p(\mathbf{s},q) + \dot{\gamma}\ \phi(\mathbf{s},q) \tag{53}$$

is minimized while satisfying the restriction induced by the yield surface:

$$\frac{\partial \mathcal{F}(\mathbf{s},q)}{\partial \mathbf{s}} = -\frac{\partial \dot{W}^p(\mathbf{s},q)}{\partial \mathbf{s}} + \dot{\gamma}\ \frac{\partial \phi(\mathbf{s},q)}{\partial \mathbf{s}} = 0 \tag{54}$$

$$\frac{\partial \mathcal{F}(\mathbf{s},q)}{\partial q} = -\frac{\partial \dot{W}^p(\mathbf{s},q)}{\partial q} + \dot{\gamma}\ \frac{\partial \phi(\mathbf{s},q)}{\partial q} = 0 \tag{55}$$

Hence, the evolution laws result in:

$$\dot{\mathbf{e}}^p = \dot{\gamma}\ \frac{\partial \phi(\mathbf{s})}{\partial \mathbf{s}} = \sqrt{\tfrac{3}{2}}\dot{\gamma}\ \mathbf{n} \tag{56}$$

$$\dot{\xi} = \dot{\gamma} \tag{57}$$

where $\dot{\gamma}$ and $\mathbf{n} = \frac{\mathbf{s}}{\|\mathbf{s}\|}$ are the plastic multiplier and the normal to the yield surface, respectively.

The corresponding loading and unloading (Kuhn-Tucker) conditions hold:

$$\dot{\gamma} > 0 \quad \phi = 0 \quad \text{Plastic loading} \tag{58}$$

$$\dot{\gamma} = 0 \quad \phi < 0 \quad \text{Elastic unloading} \tag{59}$$

$$\dot{\gamma}\phi = 0 \tag{60}$$

In plastic loading, the plastic multiplier $\dot{\gamma}$, is obtained through the consistency condition, $\dot{\phi} = 0$, as:

$$\dot{\phi}(\mathbf{s},q) = \frac{\partial \phi}{\partial \mathbf{s}} : \dot{\mathbf{s}} + \frac{\partial \phi}{\partial q}\dot{q} = \frac{\partial \phi}{\partial \mathbf{s}} : 2G\ (\dot{\mathbf{e}} - \dot{\mathbf{e}}^p) + \frac{\partial \phi}{\partial q}\frac{dq}{d\xi}\dot{\xi} = 0 \tag{61}$$

Substituting the evolution laws in Eqs. (56-57), yields:

$$\dot{\gamma} = \sqrt{\tfrac{2}{3}}\beta\ (\mathbf{n} : \dot{\mathbf{e}}) \tag{62}$$

and, thereby, the evolution law of the plastic strains can be written as:

$$\dot{\mathbf{e}}^p = \beta\ (\mathbf{n} \otimes \mathbf{n}) : \dot{\mathbf{e}} \tag{63}$$

where $\beta = 3G\ /\left(3G\ + \frac{dq}{d\xi}\right)$ and $\beta = 1$ in the particular case of perfect plasticity.

Note that, from Eqs. (56-57), it is also possible to write:

$$\dot{\xi} = \dot{e}^p_{eq} \tag{64}$$

where $e^p_{eq} = \sqrt{\frac{2}{3}}\,\|\mathbf{e}^p\|$ is the *equivalent* (plastic) strain. Thus, the isotropic hardening/softening variable yields:

$$\xi = \max\left(e^p_{eq}\right) \tag{65}$$

This given, the mechanical dissipation can be rewritten as:

$$\dot{D}_{mech} = \mathbf{s} : \dot{\mathbf{e}}^p = s\ \dot{\gamma} = \sigma_y\left(\xi\right)\ \dot{\xi} \geq 0 \tag{66}$$

being $s_{eq} = \sigma_y$ in plastic loading ($\phi = 0,\ Eq.\,(48)$).

Remark 3 *In the case of strain-softening, the total energy (per unit volume) dissipated during the fracture process, D_{mech}, within the localization band, must fulfill the equation:*

$$D_{mech} = \frac{G_f}{h} \tag{67}$$

where G_f is the Mode-II fracture energy (per unit of surface) and h is the localization band width. The total dissipation, D_{mech}, yields:

$$D_{mech} = \int_0^\infty \dot{D}_{mech}\ dt = \int_0^\infty \sigma_y\left(\xi\right)\ d\xi = \frac{\sigma_{yo}}{\delta} \tag{68}$$

being the saturation stress set to $\sigma_\infty = 0$, (see Figure 1). Thereby, the exponent of the exponential law in Eq. (50), δ, can be expressed as [19]:

$$\delta = \frac{\sigma_{yo}}{G_f} h \tag{69}$$

Remark 4 *Further generalizations considering pressure sensitive elasto-plastic models such as Druker-Prager, or orthotropic Hill's plasticity can be also accommodated into this split format.*

2.3.3 $J2-$damage

Damage models are useful for the analysis of materials that show the degradation of both stiffness and strength. In the case of metallic alloys, damage mainly affects the shear stiffness, that is, the deviatoric component of the constitutive equation. Thus, the *J2-isotropic damage model* accounts for the degradation of the mechanical properties of these materials.

The (elastic) strain energy density function reads:

$$\Psi^e = \tfrac{1}{2}\ K\ e^2_{vol} + \tfrac{1}{2}\ \left(1 - d\right)\ 2G\ \mathbf{e} : \mathbf{e} \tag{70}$$

where $0 \leqslant d \leqslant 1$ is the damage index controlling the degradation of the shear modulus. Applying Coleman's method:

$$\dot{D}_{mech} = \left(p - \frac{\partial \Psi^e}{\partial e_{vol}}\right)\ \dot{e}_{vol} + \left(\mathbf{s} - \frac{\partial \Psi^e}{\partial \mathbf{e}}\right) : \dot{\mathbf{e}} - \frac{\partial \Psi^e}{\partial d}\ \dot{d} \geq 0 \tag{71}$$

the constitutive equations of the *J2-isotropic damage constitutive model* are:

$$p = K\ e_{vol} \tag{72}$$
$$\mathbf{s} = (1-d)\ 2G\ \mathbf{e} \tag{73}$$

and the mechanical dissipation is:

$$\dot{D}_{mech} = \left(\tfrac{1}{2}\ 2G\ \mathbf{e} : \mathbf{e}\right)\ \dot{d} \geq 0 \tag{74}$$

As for $J2-$plasticity, the equivalent stress is defined as: $s_{eq} = \sqrt{\frac{3}{2}}\,\|\mathbf{s}\|$, while the equivalent strain is $e_{eq} = \sqrt{\frac{2}{3}}\,\|\mathbf{e}\|$. This given, it is useful to write the relationship between s_{eq} and e_{eq}, as:

$$s_{eq} = (1-d)\ 3G\ e_{eq} \tag{75}$$

and the mechanical dissipation as:

$$\dot{D}_{mech} = \tfrac{1}{2}\ 3G\ e_{eq}^2\ \dot{d} \geq 0 \tag{76}$$

The $J2-$damage constitutive model adopts the same yield surface defined as for $J2-$plasticity (48) as well as the same exponential law to characterize the evolution of the tensile strength (49), as shown in Figure 2.

The inelastic work reduces to:

$$\dot{W}^p(q) = q(\xi)\ \dot{\xi} \tag{77}$$

and, according to the principle of maximum dissipation, the functional to be minimized is:

$$\digamma(q) = -\dot{W}^p(q) + \dot{\gamma}\ \phi(q) \tag{78}$$

and, thereby:

$$\frac{d\digamma(q)}{dq} = -\frac{d\dot{W}^p(q)}{dq} + \dot{\gamma}\ \frac{d\phi(q)}{dq} = 0 \tag{79}$$

From the above equation, the evolution law for the softening variable, ξ, results in

$$\dot{\xi} = \dot{\gamma} \tag{80}$$

Using the consistency condition, $\dot{\phi} = 0$, the value of the multiplier turns out:

$$\dot{\gamma} = \dot{e}_{eq} \quad \rightarrow \quad \dot{\xi} = \dot{e}_{eq} \tag{81}$$

The corresponding loading and unloading (Kuhn-Tucker) conditions hold:

$$\dot{\gamma} > 0 \quad \phi = 0 \quad \text{Loading} \tag{82}$$
$$\dot{\gamma} = 0 \quad \phi < 0 \quad \text{Unloading} \tag{83}$$
$$\dot{\gamma}\phi = 0 \tag{84}$$

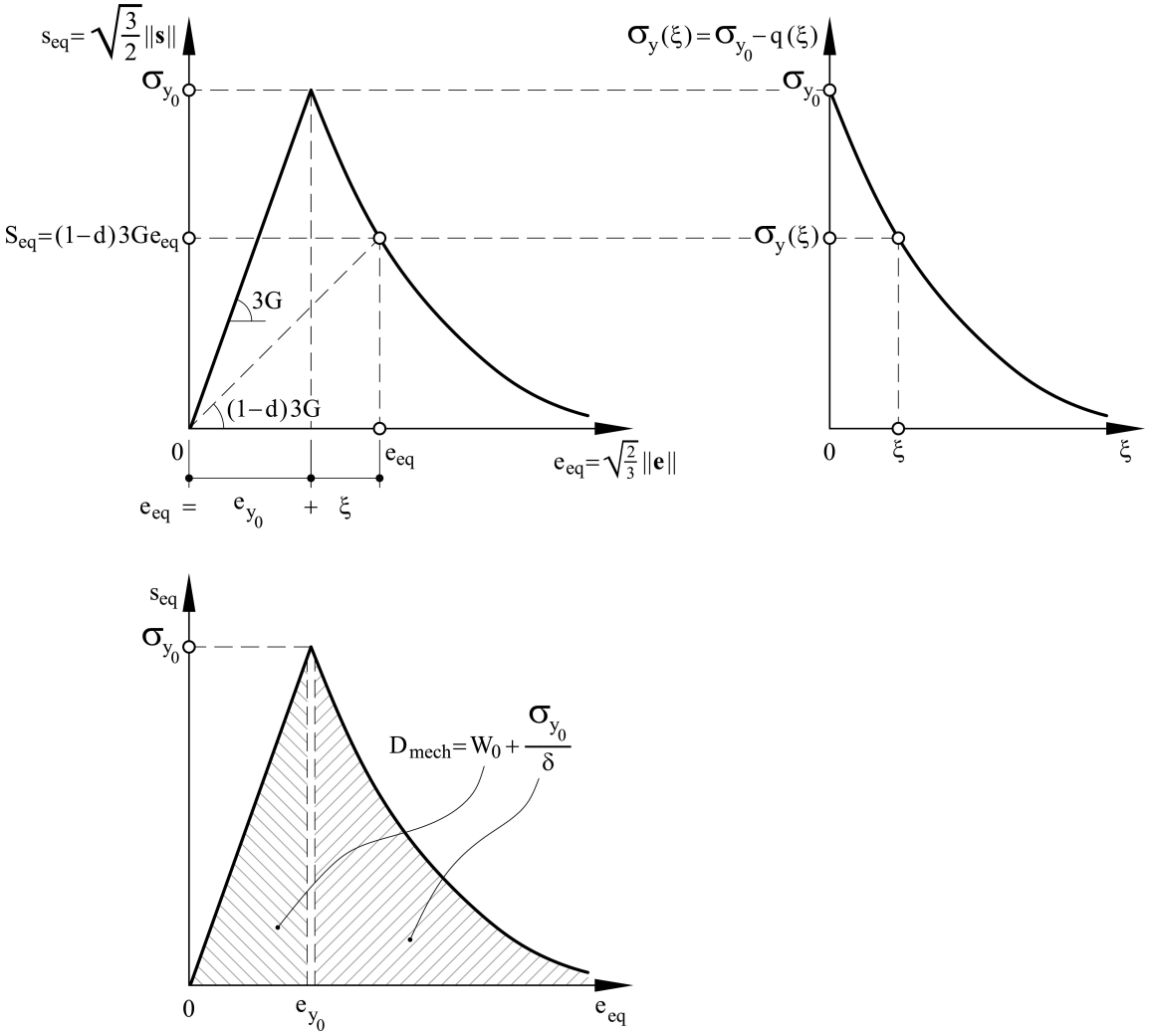

Figure 2: J2 Elasto-damage model.

Remark 5 *The tensile strength can be expressed using the equivalent definition as:*

$$\sigma_y(\xi) = (1-d)\ 3G\ (e_{yo}+\xi) \tag{85}$$

where $e_{yo} = \sigma_{yo}/3G$ is the (equivalent) strain at the elastic limit. Consequently, the yield criterion can be rewritten in a more convenient form as:

$$\phi^* = e_{eq} - (e_{yo}+\xi) \leqslant 0 \tag{86}$$

and the consistency condition, $\dot{\phi}^* = 0$, returns the expected result as shown in Eq. (81)*, and consequently: the softening variable is computed as:*

$$\xi = \max(e_{eq} - e_{yo}) \qquad e_{eq} \geq e_{yo} \tag{87}$$

The damage variable evolves once the yield criterion is satisfied: $\phi = 0$, thus:

$$\left\{ \begin{array}{c} s_{eq} = (1-d)\ 3G\ e_{eq} = \sigma_y(\xi) \\ e_{eq} = e_{yo} + \xi \end{array} \right. \quad \rightarrow \quad d = 1 - \frac{\sigma_y(\xi)}{\sigma_{yo} + 3G\ \xi} \tag{88}$$

where $\sigma_{yo} = 3G\ e_{yo}$.

Remark 6 *The total energy (per unit volume) dissipated during the fracture process is (see Figure 2):*

$$D_{mech} = \int_0^\infty \dot{D}_{mech}\ dt = W_o^e + \frac{\sigma_{yo}}{\delta} \tag{89}$$

where $W_o^e = \frac{1}{2}\frac{\sigma_{yo}^2}{3G}$ *is the modulus of resilience (maximum energy per unit volume that can be absorbed up to the elastic limit without permanent damage). According to Eq.* (67)*, the exponent of the softening law,* δ*, can be expressed as [18]:*

$$\delta = \frac{\sigma_{yo}}{G_f - W_o^e h}\, h \tag{90}$$

2.4 The 3-field formulation

The mixed $\mathbf{u}/\mathbf{e}/p$ formulation is obtained by applying the volumetric/deviatoric split to the $\mathbf{u}/\boldsymbol{\varepsilon}$ formulation $(9-10)$, as:

$$\nabla \cdot \left(\mathbb{C}^{dev} : \mathbf{e} \right) + \nabla p + \mathbf{b} = \mathbf{0} \tag{91}$$

$$\mathbb{P} : \nabla^s \mathbf{u} - \mathbf{e} = \mathbf{0} \tag{92}$$

$$\nabla \cdot \mathbf{u} - \frac{p}{C^{vol}} = 0 \tag{93}$$

where Eq. (91) is the balance of momentum equation in mixed form, including the contributions of the deviatoric stresses and the pressure, $\mathbf{s}(\mathbf{e})$ and p, respectively. Eqs. $(92-93)$ are the deviatoric and the volumetric components of the kinematic equation (10).

The *weak* form of the mixed 3−field formulation reads:

$$\int_\Omega \delta\mathbf{u}^T\ \nabla \cdot \left(\mathbb{C}^{dev} : \mathbf{e} \right)\ dV + \int_\Omega \delta\mathbf{u}^T\ \nabla p\ dV + \int_\Omega \delta\mathbf{u}^T\ \mathbf{b}\ dV = 0 \tag{94}$$

$$\int_\Omega \delta\mathbf{e}^T\ (\mathbb{P} : \nabla^s \mathbf{u})\ dV - \int_\Omega \delta\mathbf{e}^T\ \mathbf{e}\ dV = 0 \tag{95}$$

$$\int_\Omega \delta p^T\ (\nabla \cdot \mathbf{u})\ dV - \int_\Omega \delta p^T\ \frac{p}{C^{vol}}\ dV = 0 \tag{96}$$

where $\delta\mathbf{u}$, $\delta\mathbf{e}$ and δp are the test functions of the displacement, deviatoric strains and the the pressure field, respectively. Integrating Eq. (94) by parts and taking $\delta\mathbf{u} = \mathbf{0}$ on $\partial\Omega_u$, the problem

is written as:

$$\begin{array}{rcrcrcl} 0 & + & \int\limits_{\Omega} (\nabla^s \delta\mathbf{u})^T \ \left(\mathbb{C}^{dev} : \mathbf{e}\right) \ dV & + & \int\limits_{\Omega} (\nabla \cdot \delta\mathbf{u})^T \ p \ dV & = & F(\delta\mathbf{u}) \\ \int\limits_{\Omega} \delta\mathbf{e}^T \ (\mathbb{P} : \nabla^s \mathbf{u}) \ dV & - & \int\limits_{\Omega} \delta\mathbf{e}^T \ \mathbf{e} \ dV & + & 0 & = & 0 \\ \int\limits_{\Omega} \delta p^T \ (\nabla \cdot \mathbf{u}) \ dV & + & 0 & - & \dfrac{1}{C^{vol}} \int\limits_{\Omega} \delta p^T \ p \ dV & = & 0 \end{array} \tag{97}$$

where $F(\delta\mathbf{u})$ is the work of the external loads, defined as:

$$F(\delta\mathbf{u}) = \int\limits_{\Omega} \delta\mathbf{u}^T \ \mathbf{b} \ dV + \int\limits_{\partial\Omega_t} \delta\mathbf{u}^T \ \bar{\mathbf{t}} \ dS \tag{98}$$

being $\bar{\mathbf{t}}$ the prescribed tractions on $\partial\Omega_t$ (Neumann's boundary conditions).

Problem (97) involves the first derivatives of $\mathbf{u}$. Hence, the natural space for the continuum displacements is $V = H^1(\Omega)^{n_{\dim}}$. $H^m(\Omega)$ denotes the space of functions whose derivatives (up to order $m \geq 0$) belong to $L^2(\Omega)$. The corresponding variations are defined in $V_0 = \{\delta\mathbf{u}(\mathbf{X}) \in V \mid \delta\mathbf{u} = \mathbf{0} \ \text{ for } \forall \mathbf{X} \in \partial\Omega_u\}$. The natural space for the deviatoric part of the strain field $\mathbf{e}$, and its variations $\delta\mathbf{e}$, is $S = \left\{\mathbf{e}(\mathbf{X}) = [e_{ij}(\mathbf{X})], \quad e_{ij} = e_{ji} \in L^2(\Omega) \mid tr(\mathbf{e}) = 0 \ \text{ for } \forall \mathbf{X} \in \Omega\right\}$. The pressure field p, and its variation δp, belong to space $Q = L^2(\Omega)$.

Other functional settings may be considered by changing the terms integrated by parts. In fact, the formulation that yields optimal stress convergence for equal interpolation for all the unknowns requires more regularity on the stresses. We will not treat this issue in this work (see [4] for similar ideas in the context of Darcy's problem).

Problem (97) is complemented by Dirichlet's boundary conditions in terms of the prescribed displacements $\mathbf{u}(\mathbf{X}) = \bar{\mathbf{u}}$ for $\forall \mathbf{X} \in \partial\Omega_u$.

Remark 7 *To achieve symmetry, the second equation is multiplied by* $\mathbb{C}$*, and because* $\mathbb{C}^{dev} = \mathbb{P} : \mathbb{C}$*, problem* (97) *reads:*

$$\begin{array}{rcrcrcl} 0 & + & \int\limits_{\Omega} (\nabla^s \delta\mathbf{u})^T \ \left(\mathbb{C}^{dev} : \mathbf{e}\right) \ dV & + & \int\limits_{\Omega} (\nabla \cdot \delta\mathbf{u})^T \ p \ dV & = & F(\delta\mathbf{u}) \\ \int\limits_{\Omega} \delta\mathbf{e}^T \ \left(\mathbb{C}^{dev} : \nabla^s \mathbf{u}\right) \ dV & - & \int\limits_{\Omega} \delta\mathbf{e}^T \ (\mathbb{C} : \mathbf{e}) \ dV & + & 0 & = & 0 \\ \int\limits_{\Omega} \delta p^T \ (\nabla \cdot \mathbf{u}) \ dV & + & 0 & - & \int\limits_{\Omega} \delta p^T \ \dfrac{p}{C^{vol}} \ dV & = & 0 \end{array} \tag{99}$$

2.5 Discrete approximation of the 3-field problem

To obtain the discrete Galerkin Finite Element (FE) approximation of problem (99), the material domain $\Omega(\mathbf{X})$, is discretized into finite elements, $\Omega^{(e)}$, so that: $\Omega = \bigcup\limits_{e=1}^{ne} \Omega^{(e)}$, being ne, the total number of elements,

The continuum solution $\left\{ \begin{array}{cc} \mathbf{u}, & \mathbf{e}, \quad p \end{array} \right\} \in \mathbb{W} = V \times S \times Q$ is approximated by $\left\{ \begin{array}{cc} \mathbf{u}_h, & \mathbf{e}_h, \quad p_h \end{array} \right\}$ defined onto the Galerkin FE space: $\mathbb{W}_h = V_h \times S_h \times Q_h$. Thus, the discrete counterpart of the weak form of the 3−field problem is written as:

$$\begin{array}{rcrcrcr} 0 & + & \int\limits_{\Omega} (\nabla^s \delta\mathbf{u}_h)^T \ \left(\mathbb{C}^{dev} : \mathbf{e}_h\right) \ dV & + & \int\limits_{\Omega} (\nabla \cdot \delta\mathbf{u}_h)^T \ p_h \ dV & = & F\left(\delta\mathbf{u}_h\right) \\ \int\limits_{\Omega} \delta\mathbf{e}_h^T \ \left(\mathbb{C}^{dev} : \nabla^s \mathbf{u}_h\right) \ dV & - & \int\limits_{\Omega} \delta\mathbf{e}_h^T \ \left(\mathbb{C} : \mathbf{e}_h\right) \ dV & + & 0 & = & 0 \\ \int\limits_{\Omega} \delta p_h^T \ \left(\nabla \cdot \mathbf{u}_h\right) \ dV & + & 0 & - & \int\limits_{\Omega} \delta p_h^T \ \dfrac{p_h}{C^{vol}} \ dV & = & 0 \end{array} \tag{100}$$

being $\int\limits_{\Omega} (\cdot) \ dV = \bigcup\limits_{e=1}^{ne} \int\limits_{\Omega^{(e)}} (\cdot) \ dV$

Denoting by $\mathbf{U} = \left[U_i^A\right] = \left[\begin{array}{ccc} U_x^A & U_y^A & U_z^A \end{array} \right]$, $\mathbf{E} = \left[E_i^A\right] = \left[\begin{array}{cccccc} E_{xx}^A & E_{yy}^A & E_{zz}^A & E_{xy}^A & E_{xz}^A & E_{yz}^A \end{array} \right]$ and $\mathbf{P} = \left[P^A\right]$ the nodal values of the master fields, their element-wise approximation is written as:

$$\mathbf{u}_h^{(e)} = \mathbf{N}_u \mathbf{U} = \left[N^A I_{(3x3)_{ij}} U_j^A\right] \tag{101}$$

$$\mathbf{e}_h^{(e)} = \mathbf{N}_e \mathbf{E} = \left[N^A I_{(6x6)_{ij}} E_j^A\right] \tag{102}$$

$$p_h^{(e)} = \mathbf{N}_p \mathbf{P} = \left[N^A P^A\right] \tag{103}$$

where $\mathbf{N}_u = \left[N^A I_{(3x3)_{ij}}\right]$, $\mathbf{N}_e = \left[N^A I_{(6x6)_{ij}}\right]$ and $\mathbf{N}_p = \left[N^A\right]$ are the matrices incorporating the shape functions, N^A, at each node A, adopted for the FE interpolation of all master fields.

The elemental stiffness matrix of the *algebraic form* of problem (100) is:

$$\mathbb{K}_h^{(e)} = \int\limits_{\Omega^{(e)}} \left[\begin{array}{ccc} [\mathbf{0}] & \left[\mathbf{B}^T \mathbf{C}^{dev} \mathbf{N}_e\right] & [\mathbf{G}\mathbf{N}_p] \\ \left[\mathbf{N}_e^T \mathbf{C}^{dev} \mathbf{B}\right] & -\left[\mathbf{N}_e^T \mathbf{C} \mathbf{N}_e\right] & [\mathbf{0}] \\ \left[\mathbf{N}_p^T \mathbf{G}^T\right] & [\mathbf{0}] & -\frac{1}{C^{vol}} \left[\mathbf{N}_p^T \mathbf{N}_p\right] \end{array} \right] \ dV \tag{104}$$

where $\mathbf{G} = \left[G_i^A\right]$ and $\mathbf{G}^T$ stand for the (discrete) gradient and divergence matrices, while $\mathbf{B} = \left[B_{ij}^A\right]$ and $\mathbf{B}^T$ are the (discrete) symmetric gradient and divergence (applied to 2^{nd} order tensors expressed in Voigt's notation). Finally, $\mathbf{C}$ and $\mathbf{C}^{dev}$ are the rank−2 constitutive matrices and its deviatoric part, when both stresses and strains are expressed in Voigt's notation.

2.6 Variational-Multi-Scale Stabilization technique

In this work, continuous *equal order linear interpolation* for all fields is assumed. This choice does not comply with the compatibility limitations stated by the inf-sup stability condition [12]. This can be circumvented by using a *stabilization technique*. The *Variational-Multi-Scale* (VMS) method is introduced to stabilize the mixed discrete formulation and allowing for the use of linear interpolations for all master fields.

The basic idea of the VMS method consists of approximating the space $\mathbb{W}$, where the continuum solution belongs to, at two different levels of resolution (scales): a coarse FE space $\mathbb{W}_h$ and a finer

one, $\widetilde{\mathbb{W}}$. Hence, the enhanced approximation is defined as:

$$\left\{ \begin{array}{l} \mathbf{u} \simeq \mathbf{u}_h + \widetilde{\mathbf{u}} \\ \mathbf{e} \simeq \mathbf{e}_h + \widetilde{\mathbf{e}} \\ p \simeq p_h + \widetilde{p} \end{array} \right. \quad \text{in} \quad \mathbb{W} \simeq \mathbb{W}_h \oplus \widetilde{\mathbb{W}} \tag{105}$$

On the one hand, the coarse scale can be solved using the standard FE interpolation; on the other hand, the sub-grid scale cannot be solved and only its *effect* is accounted for, enhancing the stability of the mixed formulation. According to the original work of Codina [30], the sub-grid approximation is expressed in terms of the residuals of the projected (Galerkin) components of Eqs. $(91-93)$ as:

$$\widetilde{\mathbf{u}} = \tau_u \, R_u^h = \tau_u \, \left[\nabla \cdot \left(\mathbb{C}^{dev} : \mathbf{e}_h \right) + \nabla p_h + \mathbf{b} \right] \tag{106}$$

$$\widetilde{\mathbf{e}} = \tau_e \, R_e^h = \tau_e \, \left[\mathbb{P} : \nabla^s \mathbf{u}_h - \mathbf{e}_h \right] \tag{107}$$

$$\widetilde{p} = \tau_p \, R_p^h = \tau_p \, \left[\nabla \cdot \mathbf{u}_h - \tfrac{p_h}{\tilde{C}^{vol}} \right] \tag{108}$$

where the stabilization parameters ([28], [13]):

$$\tau_u = c_u \frac{hL}{2\widetilde{C}^{dev}} \tag{109}$$

$$\tau_e = c_e \frac{h}{L} \tag{110}$$

$$\tau_p = c_p \tilde{C}^{vol} \frac{h}{L} \tag{111}$$

are expressed in terms of the element size h, the characteristic length of the computational domain L, as well as two additional parameters related to the *effective* deviatoric and volumetric stuffiness of the material: the *secant* shear modulus, defined as: $2\widetilde{C}^{dev} = \|\mathbf{s}_h\| \, / \, \|\mathbf{e}_h\|$, and the *compressibility* modulus, $\tilde{C}^{vol}$. Coefficients c_u, c_e and c_p are constants to be chosen.

According to Fourier's analysis in [4], the compressibility modulus can be defined as:

$$\tilde{C}^{vol} = \left(\frac{c_1}{2\widetilde{C}^{dev}} + \frac{c_2}{C^{vol}} \right)^{-1} \tag{112}$$

where c_1 and c_2 are arbitrary constants.

Remark 8 *In isotropic elasticity,* $2\widetilde{C}^{dev} = 2G$*, and choosing* $c_1 = 1$ *and* $c_2 = 2/3$*, then:*

$$\tilde{C}^{vol} = \frac{2G}{3} \left(\frac{1+\upsilon}{1-\upsilon} \right) \quad \left\{ \begin{array}{ll} \upsilon = 0 & \tilde{C}^{vol} = \dfrac{2G}{3} = K \\ \upsilon = 0.5 & \tilde{C}^{vol} = 2G \end{array} \right.$$

The solution of the problem is approximated as:

$$\mathbf{u} \simeq \mathbf{u}_h + \widetilde{\mathbf{u}} = \mathbf{u}_h + \tau_u \, \left[\nabla \cdot \left(\mathbb{C}^{dev} : \mathbf{e}_h \right) + \nabla p_h + \mathbf{b} \right] \tag{113}$$

$$\mathbf{e} \simeq \mathbf{e}_h + \widetilde{\mathbf{e}} = (1 - \tau_e) \, \mathbf{e}_h + \tau_e \, \left[\mathbb{P} : \nabla^s \mathbf{u}_h \right] \tag{114}$$

$$p \simeq p_h + \widetilde{p} = \left(1 - \frac{\tau_p}{C^{vol}} \right) \, p_h + \tau_p \, \left[\nabla \cdot \mathbf{u}_h \right] \tag{115}$$

Remark 9 *Note that in the incompressible limit* $C^{vol} \rightarrow \infty$ *and* $\nabla \cdot \mathbf{u}_h \rightarrow 0$*; thus, the pressure field:* $p \simeq p_h$.

Introducing the approximate fields $(113-115)$ into the original problem (99), the elemental stiffness matrix of the problem, now including the VMS stabilization, is expressed as:

$$\mathbb{K}^{(e)} = \mathbb{K}_h^{(e)} - \tau_u \, \mathbb{K}_{\tau_u}^{(e)} - \tau_e \, \mathbb{K}_{\tau_e}^{(e)} - \tau_p \, \mathbb{K}_{\tau_p}^{(e)} \tag{116}$$

where there exist 3 different contributions to add stability to the Galerkin problem. The matrix form of these terms is:

$$\mathbb{K}_{\tau_u}^{(e)} = \int_{\Omega^{(e)}} \begin{bmatrix} [\mathbf{0}] & [\mathbf{0}] & [\mathbf{0}] \\ [\mathbf{0}] & \left[\left(\mathbf{C}^{dev}\mathbf{B}\right)\left(\mathbf{C}^{dev}\mathbf{B}\right)^T\right] & \left[\left(\mathbf{C}^{dev}\mathbf{B}\right)\mathbf{G}\right] \\ [\mathbf{0}] & \left[\mathbf{G}^T\left(\mathbf{C}^{dev}\mathbf{B}\right)^T\right] & [\mathbf{G}^T\mathbf{G}] \end{bmatrix} dV \tag{117}$$

$$\mathbb{K}_{\tau_e}^{(e)} = \int_{\Omega^{(e)}} \begin{bmatrix} -\left[\mathbf{B}^T\left(\mathbf{C}^{dev}\mathbf{B}\right)\right] & \left[\left(\mathbf{C}^{dev}\mathbf{B}\right)^T\mathbf{N}_e\right] & [\mathbf{0}] \\ \left[\mathbf{N}_e^T\left(\mathbf{C}^{dev}\mathbf{B}\right)\right] & -\left[\mathbf{N}_e^T\mathbf{C}\mathbf{N}_e\right] & [\mathbf{0}] \\ [\mathbf{0}] & [\mathbf{0}] & [\mathbf{0}] \end{bmatrix} dV \tag{118}$$

$$\mathbb{K}_{\tau_p}^{(e)} = \int_{\Omega^{(e)}} \begin{bmatrix} -\left[\mathbf{G}\mathbf{G}^T\right] & [\mathbf{0}] & \frac{1}{C^{vol}}\left[\mathbf{G}\mathbf{N}_p\right] \\ [\mathbf{0}] & [\mathbf{0}] & [\mathbf{0}] \\ \frac{1}{C^{vol}}\left[\mathbf{N}_p^T\mathbf{G}^T\right] & [\mathbf{0}] & -\frac{1}{\left(C^{vol}\right)^2}\left[\mathbf{N}_p^T\mathbf{N}_p\right] \end{bmatrix} dV \tag{119}$$

Remark 10 *The sub-grid scales are "small" compared to the FE scales and they vanish at a rate equal to one order higher than the FE interpolation degree. For linear elements this means that the sub-grid scales reduce with the square of the element size. Thus, the relative weight of the sub-grid scale can be used as an efficient indicator of the discretization error of a given FE mesh and it can be used as driver for adaptive mesh refinement in linear and nonlinear solid mechanics* ([3], [5]) .

3 Fluid mechanics

3.1 The continuum problem

In fluid mechanics, $\Omega(\mathbf{x})$ denotes a *spatial* domain, composed of *spatial points*, $\mathbf{x}$, and $\mathbf{u}(\mathbf{x})$ stands for the *velocity field*.

Eqs. $(1)-(3)$ define the associated mechanical problem when Cauchy's equilibrium equation (1) is assumed in its *steady-state* form. This framework is suitable for laminar flow problems characterized by very low Reynolds numbers (ratio of inertial forces to viscous forces). Thus, it is possible to neglect the inertia forces (convection), compared to the frictional shear forces due to the actual (very high) viscosity values. As shown through the numerical assessment, this is applied in incompressible *rigid-viscoplastic flows*, as typically found in many industrial manufacturing processes, such as extrusion, Friction Stir Welding (FSW) or forging.

On the one hand, the kinematic constraint to enforce the *isochoric* behavior (*incompressibility*) must be satisfied:

$$\nabla \cdot \mathbf{u} = 0 \tag{120}$$

On the other hand, the strain-rate, $\boldsymbol{\varepsilon} = \nabla^s \mathbf{u}$, is a fully deviatoric field, thus: $\boldsymbol{\varepsilon} \equiv \mathbf{e}$.

The resulting set of equations defining the continuum problem is:

$$\begin{aligned} \nabla \cdot \mathbf{s} + \boldsymbol{\nabla} p + \mathbf{b} &= \mathbf{0} && (121) \\ \mathbf{e} - \nabla^s \mathbf{u} &= \mathbf{0} && (122) \\ \nabla \cdot \mathbf{u} &= 0 && (123) \end{aligned}$$

3.2 Constitutive modeling

Two different *non-Newtonian* viscous models suitable for the analysis of rigid-viscoplastic flows are presented: Norton-Hoff and Bingham models. Both of them allow for the definition of the constitutive equation as:

$$\mathbf{s} = 2\mu_{eff}\ \mathbf{e} \tag{124}$$

where μ_{eff} is the *effective* viscosity which characterizes the specific viscous law.

In fluid mechanics, the equivalent strain-rate is defined as: $\gamma = \sqrt{2}\,\|\mathbf{e}\|$, being conjugate to the equivalent stress: $\tau = \frac{1}{\sqrt{2}}\,\|\mathbf{s}\| = \sqrt{J_2}$. Consequently, making use of the constitutive Eq. (124), the following equation holds:

$$\tau = \mu_{eff}\ \gamma \tag{125}$$

The mechanical dissipation is computed as:

$$\dot{D}_{mech} = \mathbf{s} : \mathbf{e} = \tau\ \gamma \geq 0 \tag{126}$$

3.2.1 Visco-plastic Norton-Hoff model

The Norton-Hoff model is characterized by an effective viscosity of the form:

$$\mu_{eff}\ \ (\gamma) = \mu_o\ \gamma^{m-1} \tag{127}$$

being μ_o and m the consistency parameter and the flow index, respectively. Therefore, the Norton-Hoff model is defined by the following *power law*:

$$\tau = \mu_o\ \gamma^m \quad \leftrightarrow \quad \mathbf{s} = 2\mu_o\ \gamma^{m-1}\ \mathbf{e} = 2\mu_{eff}\ \mathbf{e} \tag{128}$$

Note that for $m = 1$ the *Newtonian* behavior is recovered: $\mu_{eff} = \mu_o$, and the corresponding constitutive equation reduces to:

$$\mathbf{s} = 2\mu_o\ \mathbf{e} \tag{129}$$

3.2.2 Regularized Bingham model

The Bingham model characterizes a material that behaves as rigid at low stresses but flows as a viscous fluid under sufficiently high shear stress. The corresponding mathematical model assumes that the fluid starts flowing, with a constant viscosity μ, when the initial shear threshold, τ_{yo}, is overpassed. Thus:

$$\begin{aligned} \gamma &= 0 && \text{if} \quad \tau < \tau_{yo} \\ \gamma &= \tfrac{1}{\mu}\,(\tau - \tau_{yo}) && \text{if} \quad \tau \geq \tau_{yo} \end{aligned} \tag{130}$$

The rheological model can be written in terms of an effective viscosity, μ_{eff}, defined as:

$$\mu_{eff}\ (\gamma) = \mu + \frac{\tau_{yo}}{\gamma} \tag{131}$$

Note that when $\gamma \to 0$, this ideal rheological model presents a singularity because the effective viscosity, $\mu_{eff}(\gamma) \to \infty$. This aspect is a serious inconvenient from numerical point of view. Many authors proposed regularized versions of the Bingham model to remove this singularity ([67], [59] and [37]). In this work, the Tanner and Milthorpe model is adopted [67]. Therefore, the actual rigid behavior of the fluid when $\tau < \tau_{yo}$ is replaced by a fictitious viscosity (i.e. a regularization parameter), $\mu_o \gg \mu$, and the following bilinear form turns out:

$$\begin{array}{ll} \tau = \mu_o\ \gamma & \text{if} \quad \tau < \tau_{yo} \\ \tau = \left(\mu + \frac{\tau_{yo}}{\gamma}\right) \gamma & \text{if} \quad \tau \geq \tau_{yo} \end{array} \tag{132}$$

and the effective viscosity results in:

$$\begin{array}{ll} \mu_{eff}\ (\gamma) = \mu_o & \text{if} \quad \tau < \tau_{yo} \\ \mu_{eff}\ (\gamma) = \mu + \frac{\tau_{yo}}{\gamma} & \text{if} \quad \tau \geq \tau_{yo} \end{array} \tag{133}$$

3.3 The 3-field formulation

In this Section, the mixed $\mathbf{u}/\mathbf{e}/p$ problem (see Eqs. $91-93$) is particularized for incompressible fluids characterized by their effective viscosity, $\mu_{eff}(\gamma)$, as:

$$2\mu_{eff}\ \nabla \cdot \mathbf{e} + \nabla p + \mathbf{b} = \mathbf{0} \tag{134}$$

$$\nabla^s \mathbf{u} - \mathbf{e} = \mathbf{0} \tag{135}$$

$$\nabla \cdot \mathbf{u} = 0 \tag{136}$$

The corresponding weak form reads:

$$\begin{array}{rcccccccc} 0 & + & \int\limits_\Omega (\nabla^s \delta\mathbf{u})^T\ \left(2\mu_{eff}\ \mathbf{e}\right)\ dV & + & \int\limits_\Omega (\nabla \cdot \delta\mathbf{u})^T\ p\ dV & = & F(\delta\mathbf{u}) \\ \int\limits_\Omega \delta\mathbf{e}^T\ \left(2\mu_{eff}\ \nabla^s\mathbf{u}\right)\ dV & - & \int\limits_\Omega \delta\mathbf{e}^T\ \left(2\mu_{eff}\ \mathbf{e}\right)\ dV & + & 0 & = & 0 \\ \int\limits_\Omega \delta p^T\ (\nabla \cdot \mathbf{u})\ dV & + & 0 & - & 0 & = & 0 \end{array} \tag{137}$$

where the 2^{nd} equation has been multiplied by $2\mu_{eff}$ to achieve symmetry.

Problem (137) is complemented by Dirichlet's boundary conditions in terms of prescribed velocities, $\overline{\mathbf{u}}$.

3.4 Algebraic form

The elemental stiffness matrix of problem (137) is expressed as:

$$\mathbb{K}^{(e)} = \mathbb{K}_h^{(e)} - \tau_u\ \mathbb{K}_{\tau_u}^{(e)} - \tau_e\ \mathbb{K}_{\tau_e}^{(e)} \tag{138}$$

where the Galerkin term is:

$$\mathbb{K}_h^{(e)} = \int\limits_{\Omega^{(e)}} \begin{bmatrix} [\mathbf{0}] & 2\mu_{eff}\left[\mathbf{B}^T\mathbf{N}_e\right] & [\mathbf{G}\mathbf{N}_p] \\ 2\mu_{eff}\left[\mathbf{N}_e^T\mathbf{B}\right] & -2\mu_{eff}\left[\mathbf{N}_e^T\mathbf{N}_e\right] & [\mathbf{0}] \\ \left[\mathbf{N}_p^T\mathbf{G}^T\right] & [\mathbf{0}] & [\mathbf{0}] \end{bmatrix} dV \tag{139}$$

and the contributions adding stability to the Galerkin problem are:

$$\mathbb{K}_{\tau_u}^{(e)} = \int\limits_{\Omega^{(e)}} \begin{bmatrix} [\mathbf{0}] & [\mathbf{0}] & [\mathbf{0}] \\ [\mathbf{0}] & \left(2\mu_{eff}\right)^2\left[\mathbf{B}\mathbf{B}^T\right] & 2\mu_{eff}\left[\mathbf{B}\mathbf{G}\right] \\ [\mathbf{0}] & 2\mu_{eff}\left[\mathbf{G}^T\mathbf{B}^T\right] & \left[\mathbf{G}^T\mathbf{G}\right] \end{bmatrix} dV \tag{140}$$

$$\mathbb{K}_{\tau_e}^{(e)} = \int\limits_{\Omega^{(e)}} \begin{bmatrix} -2\mu_{eff}\left[\mathbf{B}^T\mathbf{B}\right] & 2\mu_{eff}\left[\mathbf{B}^T\mathbf{N}_e\right] & [\mathbf{0}] \\ 2\mu_{eff}\left[\mathbf{N}_e^T\mathbf{B}\right] & -2\mu_{eff}\left[\mathbf{N}_e^T\mathbf{N}_e\right] & [\mathbf{0}] \\ [\mathbf{0}] & [\mathbf{0}] & [\mathbf{0}] \end{bmatrix} dV \tag{141}$$

Therefore, the elemental stiffness matrix of the algebraic form of problem (137) including the stabilization terms reads:

$$\mathbb{K}^{(e)} = \int\limits_{\Omega^{(e)}} \begin{bmatrix} \tau_e\ 2\mu_{eff}\left[\mathbf{B}^T\mathbf{B}\right] & (1-\tau_e)\ 2\mu_{eff}\left[\mathbf{B}^T\mathbf{N}_e\right] & [\mathbf{G}\mathbf{N}_p] \\ (1-\tau_e)\ 2\mu_{eff}\left[\mathbf{N}_e^T\mathbf{B}\right] & -(1-\tau_e)\ 2\mu_{eff}\left[\mathbf{N}_e^T\mathbf{N}_e\right] - \tau_u\ \left(2\mu_{eff}\right)^2\left[\mathbf{B}\mathbf{B}^T\right] & -\tau_u\ 2\mu_{eff}\ [\mathbf{B}\mathbf{G}] \\ \left[\mathbf{N}_p^T\mathbf{G}^T\right] & -\tau_u\ 2\mu_{eff}\left[\mathbf{G}^T\mathbf{B}^T\right] & -\tau_u\ \left[\mathbf{G}^T\mathbf{G}\right] \end{bmatrix} dV \tag{142}$$

Remark 11 *Note that in the incompressible limit, the pressure field:* $p \simeq p_h$. *Therefore, the stabilization terms arising from the pressure sub-scale vanish, see Eq. (108).*

4 Numerical results

In this section, the proposed $\mathbf{u}/\mathbf{e}/p$ formulation is assessed by solving several numerical examples including both solid and fluid analyses. Different constitutive models as introduced in Sections 3 and 4 are adopted for both $2D$ and $3D$ analyses. Different FE discretizations are also tested: triangular, quadrilaterals and hexahedral elements.

The objectives are three-fold: (a) to show the faster convergence rate of the 3−field formulation over other available FE formulations, (b) to demonstrate the enhanced accuracy of the stress and strain fields over the $\mathbf{u}/p$ formulation (used as the reference solution in isochoric problems) and, as a consequence of this, (c) to show mesh bias independence when addressing strain localization problems.

The stabilization coefficients used in all examples are $c_u = 1.0$, $c_p = 1.0$ for both the $\mathbf{u}/p$ and $\mathbf{u}/\mathbf{e}/p$ formulations. The latter requires a third stabilization coefficient: $c_e = 1.0$.

The Newton-Raphson method is adopted to solve the nonlinear system of equations in an iterative and incremental manner. The number of time-steps set for all cases is 400. The convergence norm based on residual forces is 10^{-5}.

The numerical simulations are solved using an enhanced version of the in-house finite element software COMET ([14]). The pre and post processing is performed with GiD ([40]). Both softwares are developed at the International Center for Numerical Methods in Engineering (CIMNE).

4.1 Convergence test

The first example consists of a benchmark to assess the convergence rate of different finite elements formulations: standard irreducible (based on displacements, only), mixed $\mathbf{u}/p$ FE technology and the proposed mixed 3−field formulation.

The problem consists of a square domain, $\Omega = [0,1] \times [0,1]$ in $\mathbb{R}^2$, with homogeneous boundary conditions.

The exact solution is given in terms of horizontal and vertical displacements, $u(x,y)$ and $v(x,y)$, respectively defined as:

$$u(x,y) = +2x^2 y (x-1)^2 (y-1)(2y-1) \tag{143}$$
$$v(x,y) = -2xy^2 (x-1)(y-1)^2 (2x-1) \tag{144}$$

The corresponding strain field is:

$$\varepsilon_{xx}(x,y) = \frac{\partial u}{\partial x} = +4xy(x-1)(y-1)(2x-1)(2y-1) \tag{145}$$
$$\varepsilon_{yy}(x,y) = \frac{\partial v}{\partial y} = -4xy(x-1)(y-1)(2x-1)(2y-1) \tag{146}$$
$$\varepsilon_{xy}(x,y) = \frac{1}{2}\left(\frac{\partial u}{\partial y} + \frac{\partial v}{\partial x}\right) = (y-x)(x+y-1)(6x^2y - 6x^2y^2 - x^2 + 6xy^2 - 6xy + x - y^2 + y) \tag{147}$$

Note that $\varepsilon_{xx}(x,y) = -\varepsilon_{yy}(x,y)$ and, in plane strain, $\varepsilon_{zz}(x,y) = 0$. Thus, the problem is isochoric: $e_{vol} = 0$.

Assuming isotropic elasticity, the stresses are

$$\sigma_{xx}(x,y) = (\lambda + 2\mu)\varepsilon_{xx}(x,y) + \lambda\varepsilon_{yy}(x,y) \tag{148}$$
$$\sigma_{yy}(x,y) = \lambda\varepsilon_{xx}(x,y) + (\lambda + 2\mu)\varepsilon_{yy}(x,y) \tag{149}$$
$$\sigma_{xy}(x,y) = 2\mu\varepsilon_{xy}(x,y) \tag{150}$$

where $\lambda = \frac{\nu E}{(1+\upsilon)(1-2\nu)}$ and $\mu = \frac{E}{2(1+\nu)}$ are the Lamé parameters expressed in terms of the Young modulus, $E = 2,000\ MPa$ and the Poisson ratio, $\nu = 0.3$. The value of Poisson's ratio allows for using standard irreducible elements in the convergence test.

The FE discretization makes use of different structured meshes varying between 4×4 and 480×480 quadrilateral elements.

The *local* $L2$-norm of the stress field error is evaluated at each Gauss point as:

$$\|\boldsymbol{\sigma}\|_{L2}^{local} = \sqrt{\frac{(\sigma_{xx}^c - \sigma_{xx}^a)^2 + (\sigma_{yy}^c - \sigma_{yy}^a)^2 + (\sigma_{xy}^c - \sigma_{xy}^a)^2}{(\sigma_{xx}^a)^2 + (\sigma_{yy}^a)^2 + (\sigma_{xy}^a)^2}} \tag{151}$$

where the super-indexes c and a stand for the computed and analytical values, respectively. The *global* $L2$-norm is evaluated by summing the contributions at all Gauss points.

Figure 3 depicts the distribution of the local error based on the stress field. Figure 3(a) compares the 3 FE technologies (standard irreducible, mixed $\mathbf{u}/p$ and the proposed $\mathbf{u}/\mathbf{e}/p$ formulation) adopting the same mesh, while Figure 3(b) shows the error for a similar number of degrees of freedom. The accuracy of the proposed 3−field formulation is remarkable.

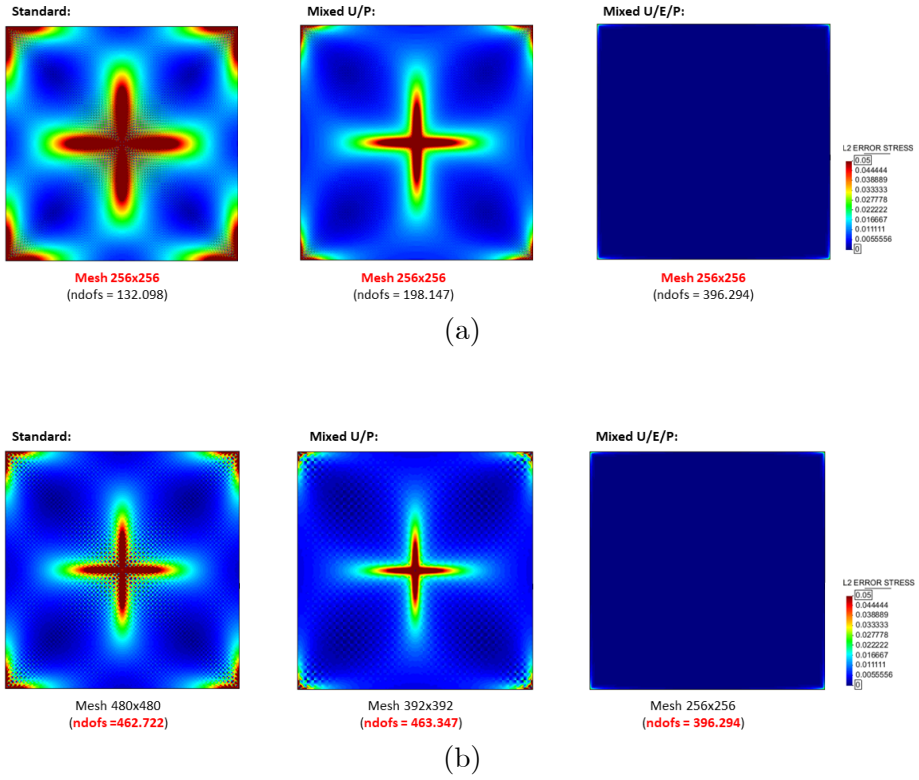

Figure 3: Local error of the stress field (L2-norm) using: (a) the same mesh; (b) similar number of degrees of freedom.

Figure 4 shows the displacement convergence rate upon mesh size. As expected the 3 FE technologies present the same slope of 2.0. More interesting is the convergence rate of the stress field. The global error is demonstrated in Figure 5. The accuracy is assessed upon mesh refinement (Figure 5(a)) and increasing the number of degrees of freedom (Figure 5(b)). The convergence rate is 1.0 for both the *standard* and the mixed $\mathbf{u}/p$ formulations while the 3−field formulation achieves the expected superior convergence rate slope of 1.5 (see [30]).

Therefore, to achieve the same accuracy, e.g. 1% of global error, both the irreducible and the $\mathbf{u}/p$ formulations require a mesh size, h, almost 10 times finer ($h \leqslant 0.003$ and $h \leqslant 0.005$, respectively) than for the 3-field FE technology ($h \leqslant 0.04$). A similar result is obtained in terms of the number of degrees of freedom (*dofs*): to get an error lower than 1%, the $\mathbf{u}/\mathbf{e}/p$ formulation

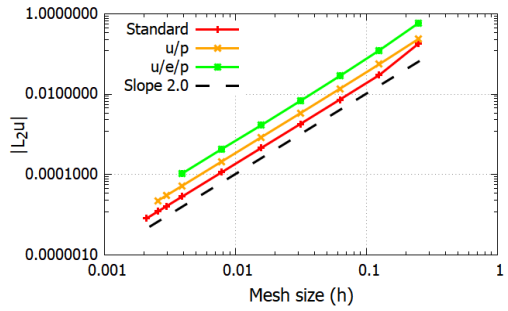

Figure 4: Convergence rate of the displacement field of the three FE technologies upon mesh refinement.

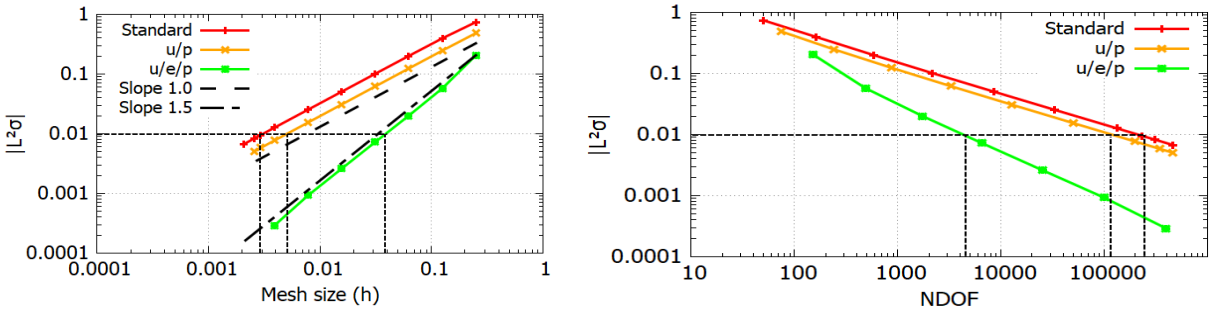

Figure 5: Convergence rate of the stress field for the three FE technologies: (a) upon mesh refinement; (b) upon number of degrees of freedom.

needs $4,292$ *dofs*, while the mixed $\mathbf{u}/p$ requires $118,150$ *dofs* (27 times more) and the standard irreducible formulation needs $211,300$ *dofs* (49 times more if compared to the 3-field and almost 2 times more than the mixed $\mathbf{u}/p$ formulation).

Figure 6 depicts the *cpu*-time needed by each FE technology to achieve a given global stress accuracy. In particular, to reduce the simulation error below 1%, the $\mathbf{u}/\mathbf{e}/p$ formulation is almost 10 time faster compared to the other technologies: $t_{\mathbf{u}/\mathbf{e}/p} \simeq 2.5 \times 10^{-4} s$, $t_{\mathbf{u}/p} \simeq 5 \times 10^{-3} s$ and $t_{\mathbf{u}} \simeq 3 \times 10^{-3} s$, respectively. The values are normalized with respect to the *cpu*-time needed for the solution of the 256×256 mesh with the $3-$field formulation.

4.2 Perforated strip

This example consists of the $2D$ plane-strain analysis of a perforated strip subjected to uniaxial stretching. The axial load is applied through a rigid plate. Because of the double symmetry, only one quarter of the domain (the top right quarter) needs to be discretized. Figure 7(a) depicts the geometry of the problem. The dimensions are relative to the size of the hole: $r = 1\ m$.

Both *J2-Plasticity* and *J2-Damage* constitutive models are adopted with a strain softening law

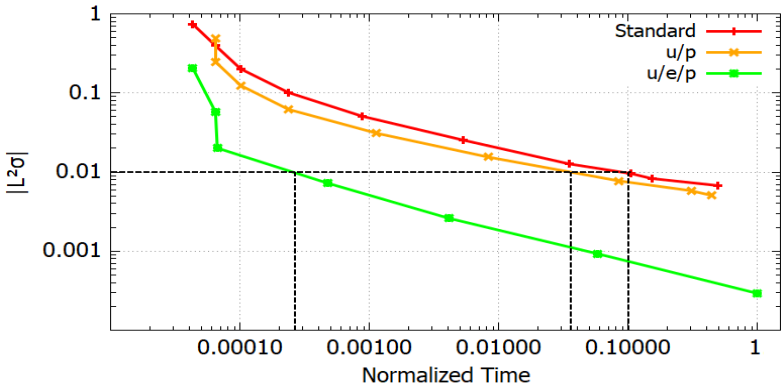

Figure 6: Convergence rate of the three FE technologies upon normalized cpu-time.

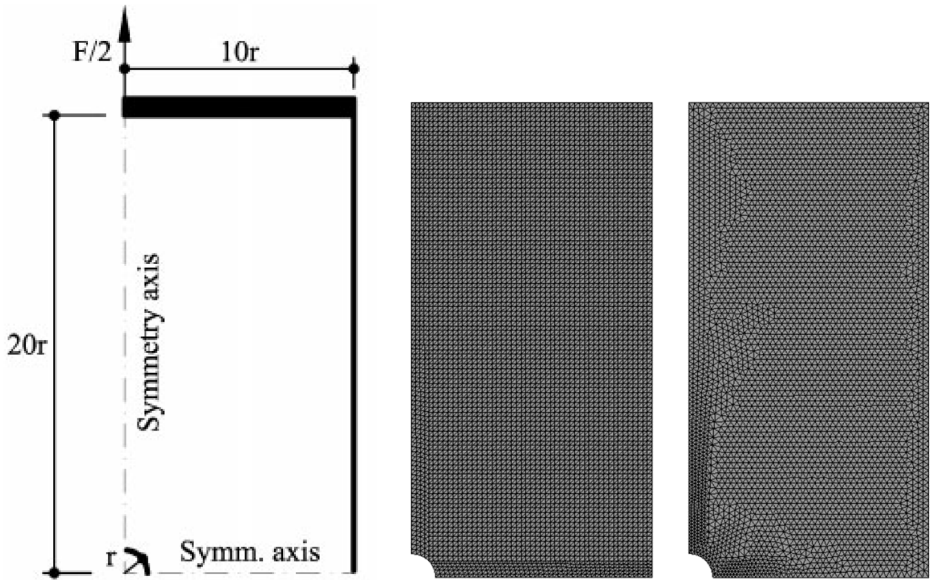

(a) Geometry (b) Structured (c) Unstructured

Figure 7: Perforated strip under uniaxial stretching.

to favor strain localization. The Young modulus of the material is $E = 10\ MPa$, the Poisson ratio $\nu = 0.5$ (incompressible elasticity), yield stress $\sigma_y = 10\ KPa$, and fracture energy $G_f = 400\ J/m^2$.

The expected failure mechanism consists of the formation of two symmetric slip-lines exactly at $\theta_{cr} = \pm 45^o$ with the horizontal axis [23]. The total amount of energy, W_{mech}, dissipated up to failure is:

$$W_{mech} = 9r \cos\theta_{cr}\ G_f = 5,091\ J \tag{152}$$

This value is used as the analytical reference to assess the accuracy of the different FE tech-

nologies used for the numerical simulation.

Figure 7(b) shows a structured mesh of $10,060$ triangular elements and $5,182$ nodes, being the average element size: $h = 0.20\ m$. This FE discretization is used to obtain the numerical *reference,* because this mesh is well-aligned with the direction of the expected slip-line.

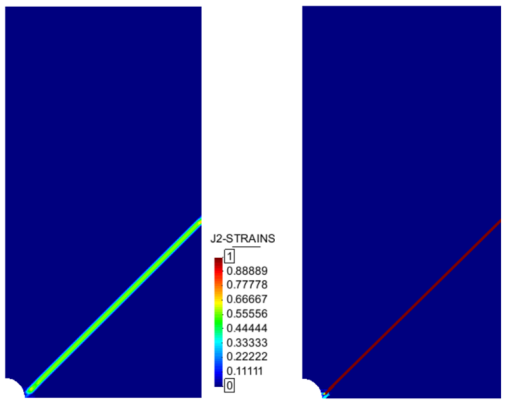

(a) u/e/p (b) u/p

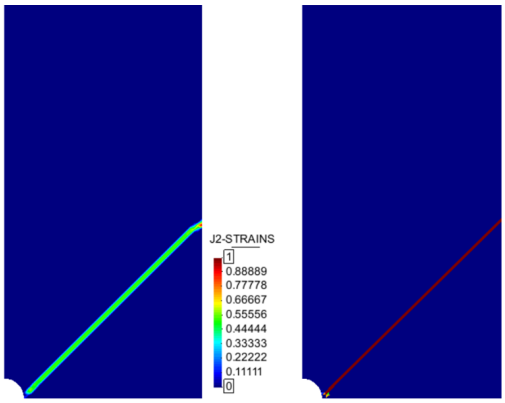

(c) u/e/p (d) u/p

Figure 8: Perforated strip. Strain localization analysis: reference results for J2-plasticity (a)-(b) and J2 damage (c)-(d).

Figure 8 shows the failure mechanism (slip-lines) obtained using the $J2$-plasticity and $J2$-damage models. Note that the strain localization is concentrated in one single element across the thickness of the shear band when the mixed $\mathbf{u}/p$ formulation is adopted (see Figures 8(b) and (d)), being the double for the $3-$field formulation (see Figures 8(a) and (c)). This is because of the different interpolation of the strain field used by the two mixed FE technologies: discontinuous and continuous strains/stresses for the $\mathbf{u}/p$ and $\mathbf{u}/\mathbf{e}/p$ formulations, respectively.

Figure 9 compares the load vs. displacement curves for all the case-studies. The curves are

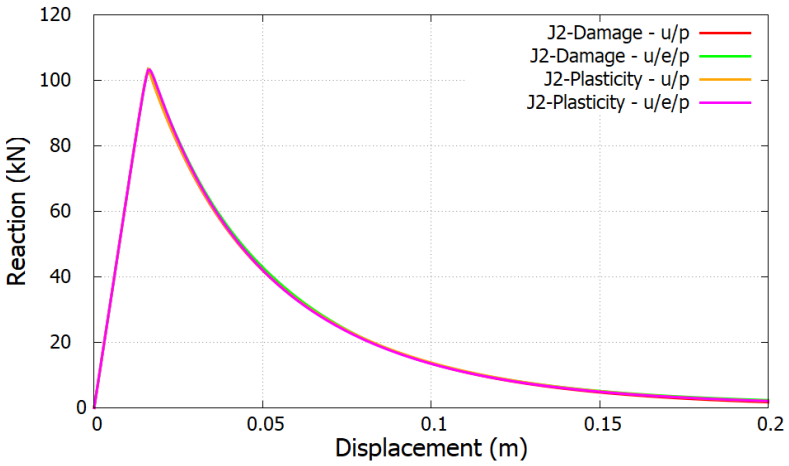

Figure 9: Perforated strip: load vs. displacement curves. Solution obtained using a structured mesh aligned with the shear band for both J2-plasticity and J2-damage models.

practically overlapped as demonstrated by the relative errors of the computed mechanical dissipation with respect to the analytical solution, as reported in Table 1. Therefore, when the mesh is aligned with the slip-lines both FE technologies predict almost the exact solution.

FE Technology	Const. Model	W_{mech} $[J]$	Error [%]
$\mathbf{u}/p$	$J2-$plasticity	$4,994$	1.91
$\mathbf{u}/p$	$J2-$damage	$4,947$	2.82
$\mathbf{u}/\mathbf{e}/p$	$J2-$plasticity	$4,991$	1.96
$\mathbf{u}/\mathbf{e}/p$	$J2-$damage	$5,053$	0.75

Table 1: Structured mesh: relative errors of the computed mechanical dissipation with respect to the analytical value.

An unstructured mesh of $7,711$ triangular elements and $3,993$ nodes with the same average element size, $h = 0.20\ m$ is analyzed next (see Figure $7(c)$). Figure 10 reports the contour-fills of the $J2$ strains corresponding to the different analyses. All results are qualitatively satisfactory, showing shear bands at $\pm 45^o$. Nevertheless, the accuracy of the different FE technologies can be appreciated in Figure 12 where the load vs. displacement curves are shown. The $3-$field formulation demonstrates its accuracy for both the $J2-$plasticity and $J2-$damage constitutive models even if an unstructured FE mesh is used. The curves are overlapped to the reference one with a small error in both cases (see Table 2).

This is not the case for the mixed $\mathbf{u}/p$ formulation. In the case of $J2-$damage, the quantitative error is small but the failure mechanism is not exactly the same, as shown by the corresponding load/displacement curve at the initiation of the shear band. The lack of accuracy is more evident for $J2-$plasticity . In Table 2 an error close to 30% is reported with respect to the reference solution, in terms of mechanical dissipation. This is due to the stress locking shown by the mixed $\mathbf{u}/p$ formulation when dealing with a directional inelastic flow, as the plastic flow in $J2-$plasticity.

FE Technology	Const. Model	W_{mech} $[J]$	Error [%]
$\mathbf{u}/p$	$J2-$plasticity	$6,538$	28.4
$\mathbf{u}/p$	$J2-$damage	$5,416$	6.4
$\mathbf{u}/\mathbf{e}/p$	$J2-$plasticity	$5,364$	5.4
$\mathbf{u}/\mathbf{e}/p$	$J2-$damage	$5,280$	3.7

Table 2: Unstructured mesh: relative errors on the computed mechanical dissipation with respect to the analytical value.

This is due to the poor performance of low order standard FE for reproducing opening or sliding modes which are not normal or paraller, respectively, to one of the sides of the element. In Figure 11, the spurious stresses at the end when the shear band is fully formed can be appreciated. Note that the $\mathbf{u}/\mathbf{e}/p$ formulation performs very well, while stress release does entirely occur for the mixed $\mathbf{u}/p$ formulation in conjunction with incremental $J2-$plasticity (see Figure 11(b)). For the $\mathbf{u}/p$ formulation in conjunction with $J2-$damage, the spurios strains do not translate into spurious streeses because of the secant format of the constitutive model and scalar damage.

4.3 Perforated thin-wall cylinder

As a third example, a thin-wall cylinder, 30 m height with an outer diameter of 6 m and a wall thickness of 0.2 m is addressed. The cylinder has a $0.40\times$ 0.40 m^2 perforation at mid-height and it is subjected to vertical stretching by an imposed vertical displacement, $\delta_z = 0.20$ m applied to the top boundary. Due to the double symmetry of the problem, only one quarter of the domain is considered (see Figure 13).

A uniform structured FE mesh is generated including $3,749$ hexahedral elements and $7,750$ nodes (see Figure 13). This discretization consists of $31,000$ *dofs* and $77,500$ *dofs* for the $\mathbf{u}/p$ and the $\mathbf{u}/\mathbf{e}/p$ formulations, respectively.

A fully incompressible ($\nu = 0.5$) elasto-*J2*-damage constitutive model is adopted including the same softening law and the same material properties as in the previous problem.

The radial stresses through the wall are null, so that planes stress conditions apply in the problem. A slip-line is expected to start from the perforation, with an angle of $\theta_{cr} = 35.26^o$ with respect to the an horizontal plane, to later develop showing a helicoidal shape and causing the failure of the structure [23].

The total amount of energy $W_{mech} = AG_f$, dissipated up to the failure is:

$$W_{mech} = h\left(\frac{\pi\phi_{mean}/2 - h}{\cos\theta_{cr}}\right) G_f = 873\ J \tag{153}$$

where ϕ_{mean} is the average diameter of the cylinder and A is the fracture surface, computed by multiplying the thickness of the cylinder by the length of the shear band (see Figure 14).

Figure 15 shows the failure mechanism (slip-line) at the end of the strain localization process for the mixed $\mathbf{u}/\mathbf{e}/p$ and the $\mathbf{u}/p$ formulations, respectively. Once again, both results are qualitatively good, being the mixed $\mathbf{u}/p$ solution sharper ($b = h$) than the one obtained by the $3-$field formulation ($b = 2h$), being b, the shear band width.

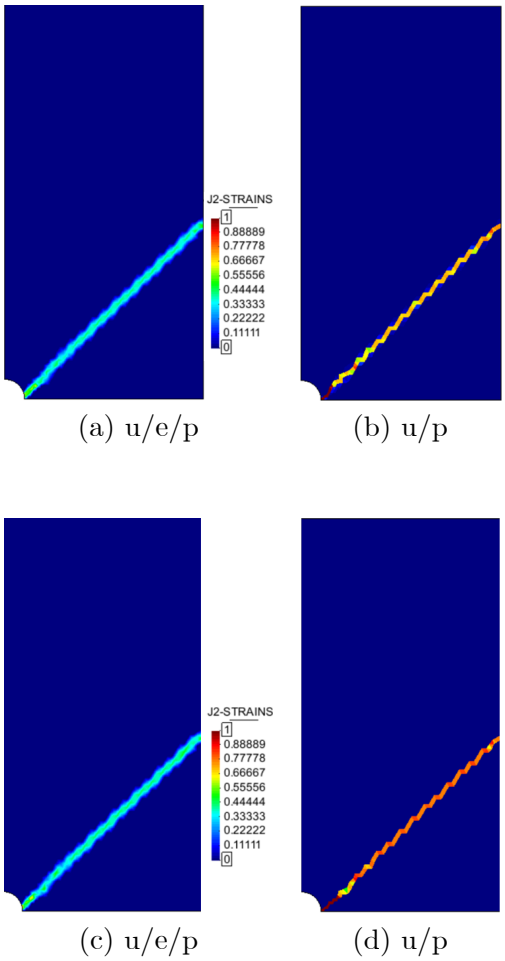

(a) u/e/p (b) u/p

(c) u/e/p (d) u/p

Figure 10: Perforated strip. Strain localization obtained with the unstructured mesh for J2-plasticity (a)-(b) and J2 damage (c)-(d).

Nevertheless, in Figure 16, it is possible to appreciate the differences found in the load vs. displacement curves recorded for both analyses. The shear band obtained with the mixed $\mathbf{u}/p$ elements is discontinuous at some instances. Contrarily, the 3−field formulation is able to generate a well defined solution during the entire analysis (see Figure 17). The accuracy of the two formulations is also reflected in the load/displacement curves. The energy dissipated by the 3−field formulation is almost exact, while the mixed $\mathbf{u}/p$ produces an error close to 30%, as shown in Table 3.

Table 3 also shows the value of the critical angle θ_{cr}, that is the slope of the shear band starting at the perforation. Once again, the accuracy of the mixed $\mathbf{u}/\mathbf{e}/p$ formulation is remarkable.

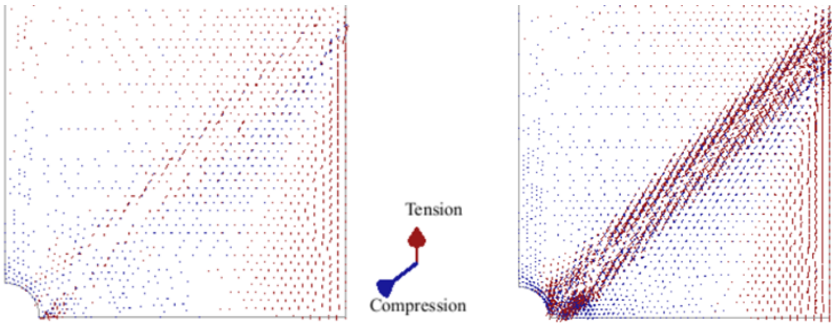

(a) u/e/p - J2 plasticity (b) u/p - J2 plasticity

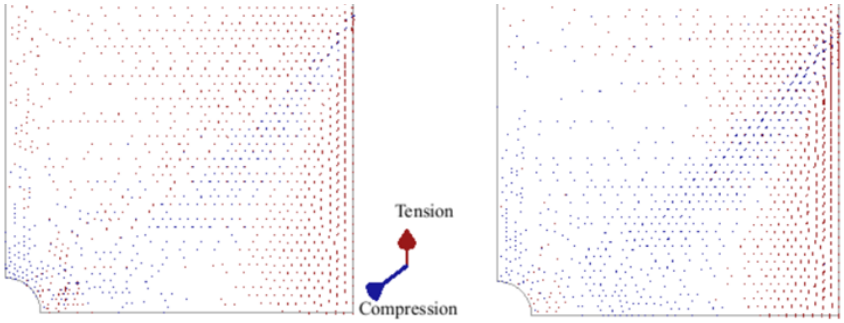

(c) u/e/p - J2 damage (d) u/p - J2 damage

Figure 11: Residual (principal) stresses at the end of the loading process when the unstructured mesh is used.

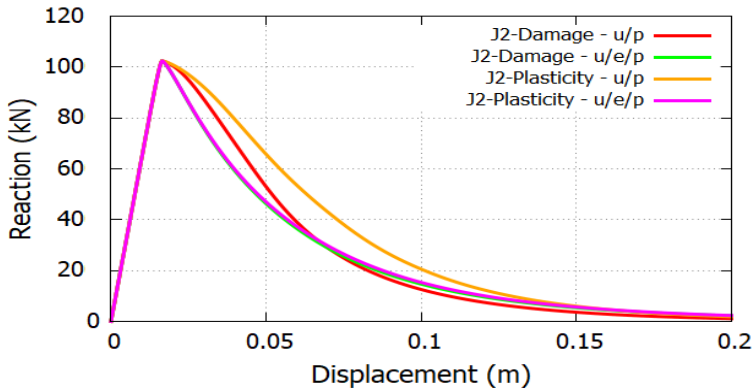

Figure 12: Perforated strip: load vs. displacement curves. Solution obtained using the unstructured mesh for both J2-plasticity and J2-damage models.

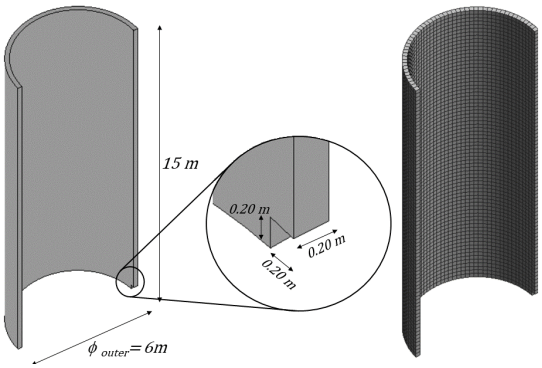

Figure 13: Perforated thin-wall cylinder: geometry and FE mesh.

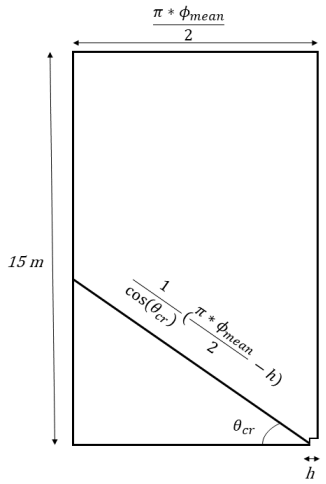

Figure 14: Perforated thin-wall cylinder: lenght of the shear band.

4.4 Elasto-plastic extrusion

Extrusion is a manufacturing process suitable to multifold engineering applications ranging from metal forming processes to the food industry.

The numerical example proposed here consists of a $2:1$ reduction direct extrusion, where a displacement, $\delta_x = 0.10\ m$ is applied through the piston. Figure 18 shows the $3D$ geometry of the problem and the corresponding dimensions. Note that due to the double symmetry conditions of the problem, one quarter of the total domain is simulated.

According to Hill's solution [41], two shear bands at $\pm 45^o$ and a slip-surface defined by a quarter circumference are expected, once the extrusion mechanism is fully developed as shown in Figure 19. The mechanical dissipation, $W_{mech} = AG_f$, is computed as:

$$W_{mech} = \left(2 + \frac{\pi}{2}\right) Rd\ G_f = 25.3\ J \tag{154}$$

where the radius of the slip-line is: $R = H\sqrt{2}$, being $H = 0.125\ m$ and $d = 0.1\ m$.

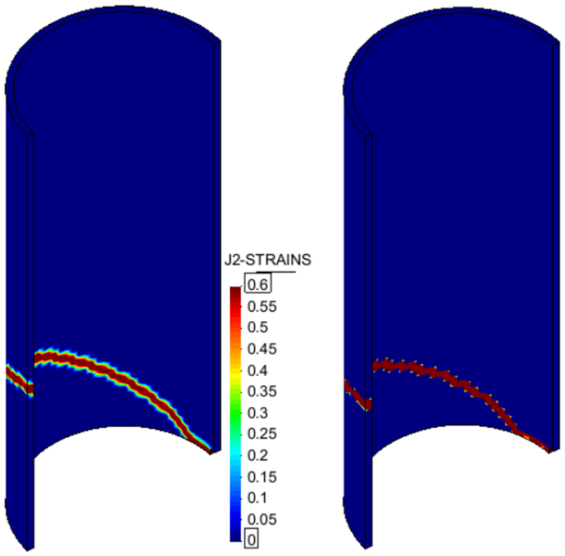

(a) u/e/p (b) u/p

Figure 15: Perforated thin-wall cylinder. Strain localization analysis: (a) Mixed u/e/p, (b) Mixed u/p formulation.

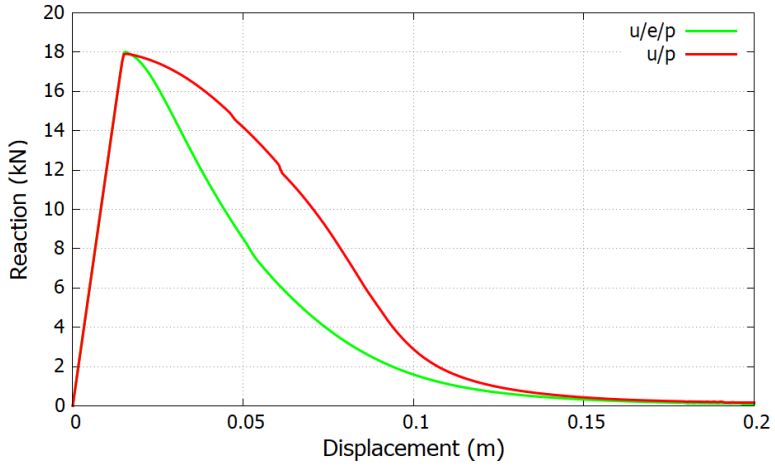

Figure 16: Perforated thin-wall cylinder: load vs. displacement curves.

An incompressible ($\nu = 0.5$) elasto$-J2-$plastic constitutive model is adopted, including the same softening law and the same material properties as in the previous problems.

A fully structured hexahedral FE mesh is generated, made of $18,227$ nodes and $15,600$ elements of an average size, $h = 0.01\ m$ (see Figure 18). Both mixed $\mathbf{u}/p$ and $\mathbf{u}/\mathbf{e}/p$ formulation are tested and compared.

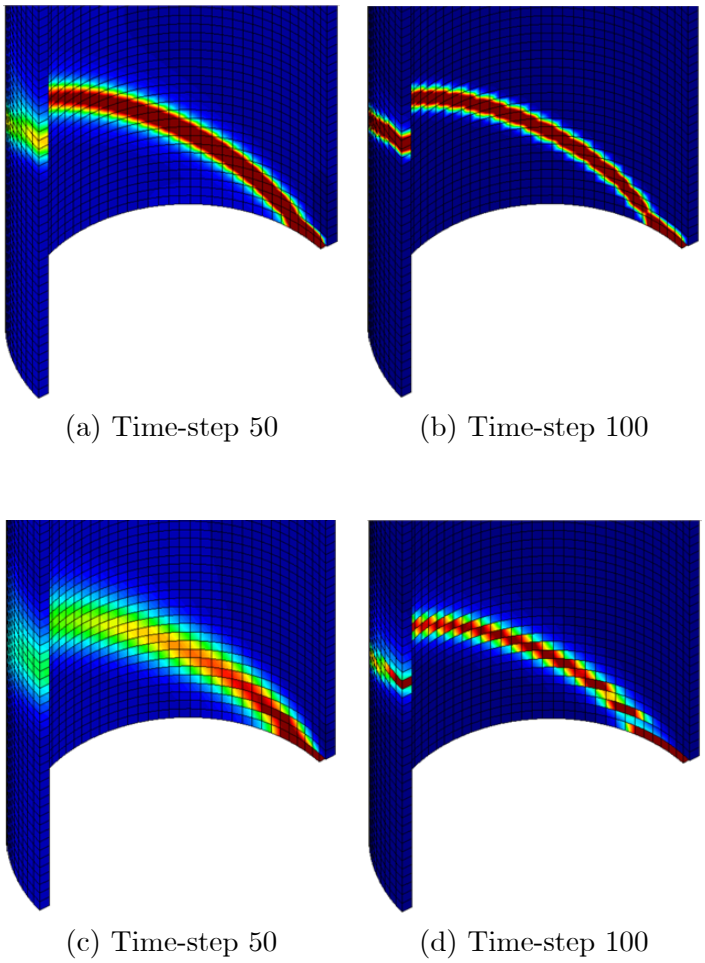

(a) Time-step 50 (b) Time-step 100

(c) Time-step 50 (d) Time-step 100

Figure 17: Strain localization at different time-steps: u/e/p formulation in (a)-(b) and u/p formulation in (c)-(d).

Figure 20 shows the two shear bands as obtained by the mixed $\mathbf{u}/\mathbf{e}/p$ and mixed $\mathbf{u}/p$ formulations. Once again, the accuracy of the solution given by the $3-$field analysis is remarkable: the slope of the shear bands is almost exact (46.12^o) despite the coarse mesh used (see Table 4). Figure $21(a)$ shows the well defined slip surface, less sensitive to the background mesh than for the $\mathbf{u}/p$ formulation (see Figure $21(b)$).

Figure 22 shows the extrusion force as a function of the imposed displacement at the piston surface. Both FE technologies are able to capture correctly the peak load. Nevertheless, the mechanical dissipation (e.g. heat generated by the plastic deformation) is over-estimated by the $\mathbf{u}/p$ formulation as reported in Table 4.

FE Technology	W_{mech} $[J]$	Error [%]	θ_{cr}	Error [%]
$\mathbf{u}/p$	$1,222$	39.98	32.17^o	8.8
$\mathbf{u}/\mathbf{e}/p$	874	0.11	35.05^o	0.6

Table 3: Difference between mixed FE formulations and analytical values.

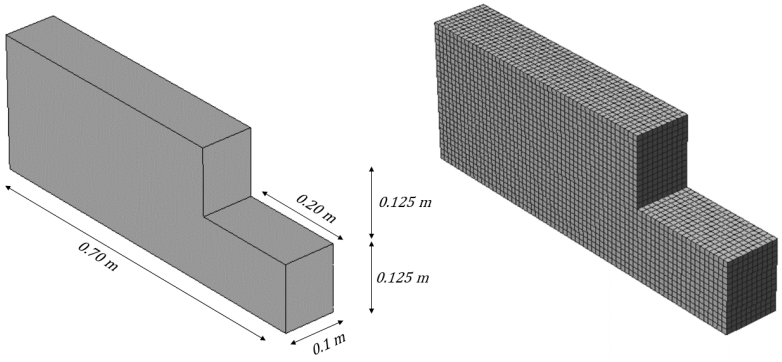

Figure 18: Elasto-plastic extrusion: geometry and FE mesh.

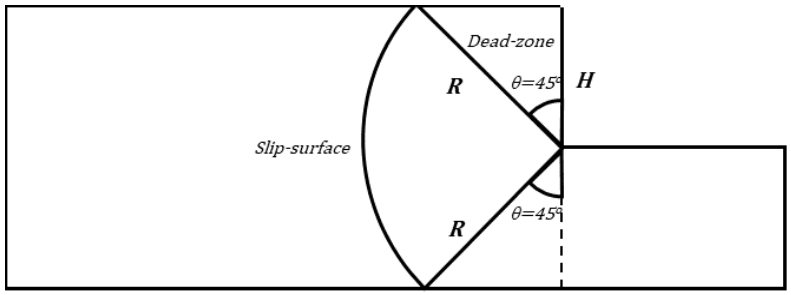

Figure 19: Elasto-plastic extrusion with 2:1 reduction.

4.5 Rigid-viscoplastic extrusion

In this example, an extrusion problem is also addressed, but now an Eulerian framework is adopted [52]. A rigid-viscoplastic Bingham model is characterized by an initial shear threshold, $\tau_{yo} = 1,000$ Pa. The constitutive model makes use of an initial viscosity (regularization parameter): $\mu_o = 10^6$ $Pa \cdot s$.

The analysis consists of a direct extrusion process characterized by a $3:1$ reduction, as shown in Figure 23. The problem is solved in $2D$ plane-strain conditions and only half of the actual geometry is analyzed because of the existing symmetry conditions.

The FE mesh consists of $2,821$ nodes and $5,340$ triangular elements with an average size of 0.1 m. Both the mixed $\mathbf{u}/p$ and the $\mathbf{u}/\mathbf{e}/p$ formulations are analyzed.

The extrusion pressure, p_{extr}, is given by [41]:

$$p_{extr} = \frac{4}{3}\left(\frac{\pi}{2} + 1\right)\tau_y = 3,428\ Pa \tag{155}$$

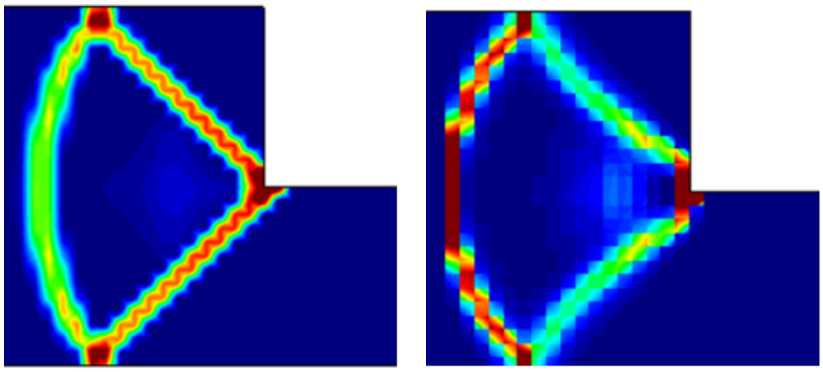

(a) u/e/p (b) u/p

Figure 20: Elasto-plastic extrusion: shear bands obtained through the numerical simulations.

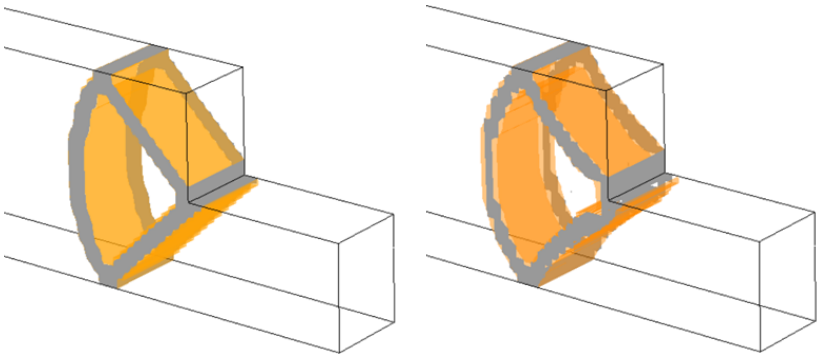

(a) u/e/p (b) u/p

Figure 21: Elasto-plastic extrusion: slip-surface and shear bands obtained through the numerical simulations.

and the expected failure mechanism is shown in Figure 24.

Figure 25 shows the streamlines and the yield region, once the extrusion mechanism is fully developed. The agreement with the analytical result is remarkable. A smoother solution is achieved with the 3−field formulation (Figure 25(a)), although the $\mathbf{u}/p$ formulation also achieves good definition in this very fine mesh. The value of the extrusion pressure predicted by both FE technologies is almost exact (see Table 5). Note that this value follows from the failure mechanism and the flow stress.

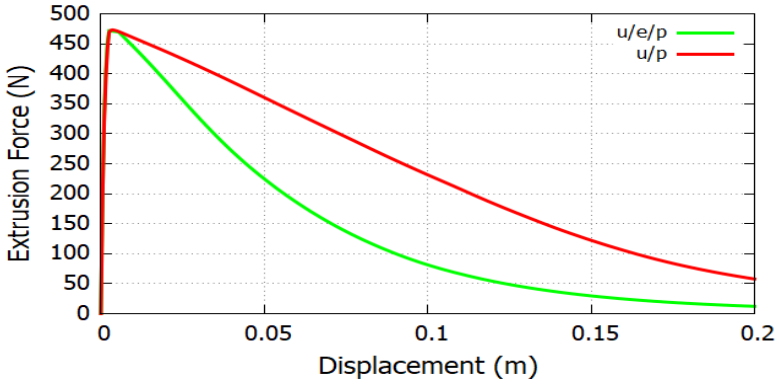

Figure 22: Elasto-plastic extrusion: Force vs Displacement curve.

FE Technology	W_{mech} $[J]$	Error [%]	θ_{cr}	Error [%]
$\mathbf{u}/p$	47.7	88.54	48.6^o	8.00
$\mathbf{u}/\mathbf{e}/p$	27.3	7.91	46.12^o	2.49

Table 4: Elasto-plastic extrusion: relative errors of both the mechanical dissipation and the shear-band angles with respect to the analytical values.

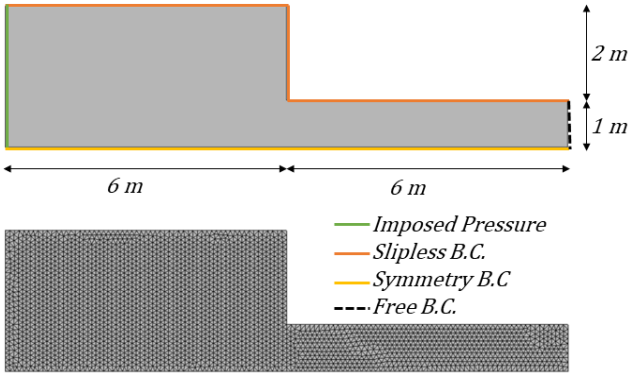

Figure 23: Rigid-viscoplastic extrusion: Problem setting and FE mesh.

5 Concluding remarks

Tis paper exploits the accuracy of the proposed 3−field formulation to tackle highly non-linear problems including isochoric elastic (incompressible elasticity) and inelastic deformations while, at the same time, achieving a remarkable degree of accuracy of both the stress and the strain fields and, ensuingly, the mechanical work and the dissipated energy.

The mixed $\mathbf{u}/\mathbf{e}/p$ formulation is developed, being suitable for several constitutive equations in Solid Mechanics (e.g. $J2-$plasticity, Drucker-Prager, $J2-$damage, etc..) and Fluid Dynamics (e.g. non-Newtonian rigid-viscoplastic flows).

The proposed 3−field formulation is convergent upon mesh refinement with a convergence rate

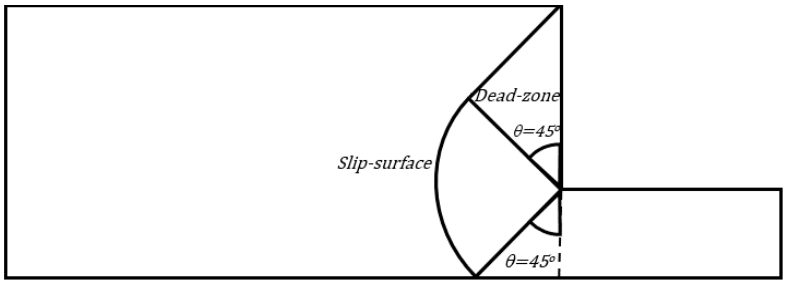

Figure 24: Expected slip-lines during the extrusion process.

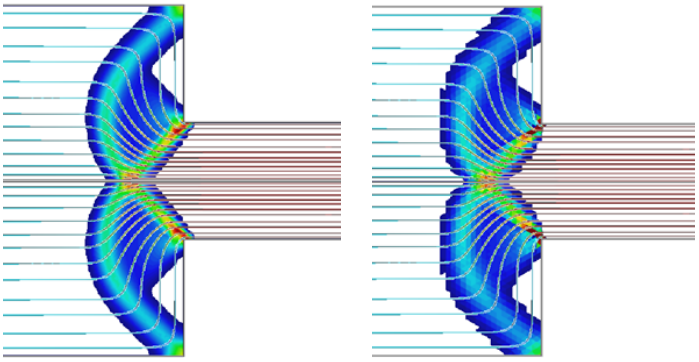

(a) u/e/p (b) u/p

Figure 25: Rigid-viscoplastic extrusion: Streamlines and yield region.

higher than the well-known mixed $\mathbf{u}/p$ formulation. Regarding efficiency,for a given accuracy, faster convergence is attained in terms of mesh refinement, degrees of freedom and cpu-time.

Several strongly non-linear problems including strain localization and the formation of shear bands are solved in $2D$ and $3D$ using triangular and quadrilateral meshes to demonstrate that the obtained solutions are free of any volumetric or shear locking.

The remarkable degree of accuracy makes the proposed mixed $\mathbf{u}/\mathbf{e}/p$ formulation very appealing for the solution of engineering problems including many industrial manufacturing processes (e.g. extrusion, forging, Additive Manufacturing, Friction Stir Welding, among others).

FE Technology	Extrusion pressure $[Pa]$	Error [%]
$\mathbf{u}/p$	$3,410.9$	0.50
$\mathbf{u}/\mathbf{e}/p$	$3,408.4$	0.58

Table 5: Extrusion pressure: relative errors with respect to the analytical value.

6 Acknowledgments

The financial support from the Spanish Ministry of Economy and Competitiveness, through the *Severo Ochoa Programme for Centres of Excellence in R&D* (CEX2018-000797-S), is gratefully acknowledged.

The authors also acknowledge the financial support provided by the Spanish Ministry of Economy via the *ADaMANT* project (DPI2017-85998-P): Computational Framework for Additive Manufacturing of Titanium Alloy, as well as the support provided by the Spanish Ministry of Education to Mr. Gabriel Barbat via the *FPU* program.

References

[1] Agelet de Saracibar C., Chiumenti M., Valverde Q., and Cervera M., On the Orthogonal Subgrid Scale Pressure stabilization of Small and Finite deformation J2 Plasticity, Computer Methods in Applied Mechanics and Engineering, (2006), 195: 1224–1251

[2] Babuška I., Error-bounds for finite element method. Numerische Mathematik, (1971), 16(4): 322–333.

[3] Baiges, J. and and Codina, R., Variational Multiscale error estimators for solid mechanics adaptive simulations: an Orthogonal Subgrid Scale approach, Computer Methods in Applied Mechanics and Engineering, (2017), 325: 37–55

[4] Badia, S. and Codina, R. Unified stabilized finite element formulations for the Stokes and the Darcy problems, SIAM Journal on Numerical Analysis (2009), 17: 309–330.

[5] Bayona, C., Codina R. and Baiges, J., Variational Multiscale error estimators for the adaptive mesh refinement of compressible flow, Computer Methods in Applied Mechanics and Engineering, (2018), 337: 501–526, https://doi.org/10.1016/j.cma.2018.03.010

[6] Benedetti, L., Cervera, M. and Chiumenti, M., Stress-accurate mixed FEM for soil failure under shallow foundations involving strain localization in plasticity, Computers and Geotechnics (2015), 64: 32–47, *https://doi.org/10.1016/j.compgeo.2014.10.004*

[7] Benedetti, L., Cervera, M. and Chiumenti, M., High-fidelity prediction of crack formation in 2D and 3D pullout tests, Computers and Structures (2016), 172: 93–109, *http://dx.doi.org/10.1016/j.compstruc.2016.05.001*

[8] Benedetti, L., Cervera, M. and Chiumenti, M., 3D Numerical Modelling of Twisting Cracks Under Bending and Torsion of Skew Notched Beams, Engineering Fracture Mechanics (2017), 176: 235–256, *http://dx.doi.org/10.1016/j.engfracmech.2017.03.025*

[9] Bonet, J. and Burton, A.J., A simple average nodal pressure tetrahedral element for incompressible and nearly incompressible dynamic explicit applications, Commun. Numer. Methods Eng. (1998), 14 (5): 437–449.

[10] Bonet, J., Marriott and H. Hassan, O., Stability and comparison of different linear tetrahedral formulations for nearly incompressible explicit dynamic applications, Internat. J. Numer. Methods Engrg. (2001), 50(1): 119–133.

[11] Bonet, J. Gil, A.J, Ortigosa, R., A computational framework for polyconvex large strain elasticity, Computer Methods in Applied Mechanics and Engineering (2015), 283:1061-1094.

[12] Brezzi F, Fortin M., Mixed and Hybrid Finite Element Methods (1st edn), Springer Series in Computational Mathematics, vol. 15. Springer, New York, 1991.

[13] Castillo, E. and Codina, R., Variational multi-scale stabilized formulations for the stationary three-field incompressible viscoelastic flow problem, Comp. Meth. in Appl. Mech. and Eng. (2014), 279: 579-605.

[14] Cervera, M., Agelet de Saracibar, C. and Chiumenti, M. COMET: COupled MEchanical and Thermal analysis. Data Input Manual, Version 5.0, Technical report IT-308, htpp://www.cimne.upc.es, (2002).

[15] Cervera, M., Chiumenti, M., Valverde, Q. and Agelet de Saracibar, C. Mixed Linear/linear Simplicial Elements for Incompressible Elasticity and Plasticity, Comp. Meth. in Appl. Mech. and Eng. (2003), 192: 5249–5263

[16] Cervera, M., Chiumenti, M. and Agelet de Saracibar, C. Softening, localization and stabilization: capture of discontinuous solutions in J2 plasticity, Int. J. for Num. and Anal. Meth. in Geomechanics (2004), 28: 373–393

[17] Cervera, M., Chiumenti, M. and Agelet de Saracibar, C. Shear band localization via local J_2 continuum damage mechanics, Comp. Meth. in Appl. Mech. and Eng. (2004), 193, 849–880.

[18] Cervera, M., Chiumenti, M., Smeared crack approach: Back to the original track, International Journal for Numerical and Analytical Methods in Geomechanics (2006), 30(12): 1173-1199.

[19] Cervera, M. and Chiumenti, M. Size effect and localization in J_2 plasticity, Int. J. of Solids and Structures (2009), 46: 3301-3312.

[20] Cervera, M., Chiumenti, M. and Codina, R. Mixed stabilized finite element methods in nonlinear solid mechanics. Part I: formulation, Comp. Meth. in Appl. Mech. and Eng. (2010), 199: 2559–2570

[21] Cervera, M., Chiumenti, M. and Codina, R. Mixed stabilized finite element methods in nonlinear solid mechanics. Part II: strain localization, Comp. Meth. in Appl. Mech. and Eng. (2010), 199: 2571–2589.

[22] Cervera, M., Chiumenti, M. and Codina, Mesh objective modeling of cracks using continuous linear strain and displacement interpolations, International Journal for Numerical Methods in Engineering (2011), 87: 962–987, *https://doi.org/10.1002/nme.3148*

[23] Cervera, M., Chiumenti, M.,Benedetti, L. and Codina, Mixed stabilized finite element methods in nonlinear solid mechanics. Part III: Compressible and incompressible plasticity, Computer Methods in Applied Mechanics and Engineering (2015) 285: 752-775, *https://doi.org/10.1016/j.cma.2014.11.040*

[24] Cervera M., Lafontaine, N., Rossi, R. and Chiumenti, M., Explicit mixed strain-displacement finite elements for compressible and quasi-incompressible elasticity and plasticity, Computational Mechanics (2016), 58(3): 511–532, *http://dx.doi.org/10.1007/s00466-016-1305-z*

[25] Cervera, M., Barbat, G.B. Chiumenti M., Finite element modeling of quasi-brittle cracks in 2D and 3D with enhanced strain accuracy, Computational Mechanics (2017), 60: 767–796, *https://doi.org/10.1007/s00466-017-1438-8*

[26] Chiumenti, M., Valverde, Q., Agelet de Saracibar, C. and Cervera, M. A stabilized formulation for incompressible elasticity using linear displacement and pressure interpolations, Comp. Meth. in Appl. Mech. and Eng. (2002), 191: 5253–5264

[27] Chiumenti, M., Valverde, Q., Agelet de Saracibar, C. and Cervera, M. A stabilized formulation for incompressible plasticity using linear triangles and tetrahedra, Int. J. of Plasticity (2004), 20: 1487–1504.

[28] Chiumenti, M.,Cervera,M. and Codina R., A mixed three-field FE formulation for stress accurate analysis including the incompressible limit, Computer Methods in Applied Mechanics and Engineering (2015), 283: 1095–1116, *https://doi.org/10.1016/j.cma.2014.08.004*

[29] Codina, R. Stabilization of incompressibility and convection through orthogonal sub-scales in finite element methods, Comp. Meth. in Appl. Mech. and Eng. (2000), 190: 1579–1599.

[30] Codina, R. Finite element approximation of the three field formulation of the Stokes problem using arbitrary interpolations, SIAM Journal on Numerical Analysis (2009), 47: 699–718.

[31] Coleman B.D., Noll W., The thermodynamics of elastic materials with heat conduction and viscosity, Arch Ration Mech (1963), 13(1): 167–178.

[32] de Souza Neto, E.A., Peric, D. Huang, G.C., Owen, D.R.J., Remarks on the stability of enhanced strain elements in finite elasticity and elastocplasticity, Commun. Numer. Methods. Eng. (1995), 11(11): 951–961.

[33] de Souza Neto, E.A., Peric, D., Dutko, M., Owen, D.R.J., Design of simple low order finite elements for large strain analysis of nearly incompressible solids, Int. J. Solids Struct. (1996), 33(20–22): 3277–3296.

[34] de Souza Neto, E.A., Andrade Pires, F.M., Owen, D.R.J., F-bar-based linear triangles and tetrahedra for finite strain analysis of nearly incompressible solids. Part I: Formulation and benchmarking, Internat. J. Numer. Methods Engrg. (2005),62 (3): 353–383.

[35] Dohrmann, C.R., Heinstein, M.W.Jung, J. Key, S.W. and Witkowski,W.R., Node-based uniform strain elements for three-node triangular and four-node tetrahedral meshes, Internat. J. Numer. Methods Engrg., (2000), 47 (9): 1549–1568.

[36] Gee, M.W., Dohrmann, C.R. , Key, S.W. and Wall,W.A., A uniform nodal strain tetrahedron with isochoric stabilization, Internat. J. Numer. Methods Engrg. (2009), 78 (4): 429–443.

[37] dos Santos, D.D., Frey, S. Naccache, M.F. and de Souza Mendes, P.R., Numerical approximations for flow of viscoplastic fluids in a lid-driven cavity, Journal of Non-Newtonian Fluid Mechanics (2011), 166(12–13): 667–679.

[38] Franca, L. P., Hughes, T.J.R., Two classes of mixed finite element methods, Comput. Methods Appl. Mech. Engrg. (1988), 69 (1): 89–129.

[39] Franca, L.P., Hughes, T.J.R. , Loula, A. F.D. and Miranda, I., A new family of stable elements for nearly incompressible elasticity based on a mixed Petrov-Galerkin finite element formulation, Numerische Mathematik, (1988), 53: 123–141.

[40] Coll, A.; Ribó, R.; Pasenau, M.; Escolano, E.; Perez, J.Suit.; Melendo, A.; Monros, A. and Gárate, J., GiD v.13 Reference Manual, (2016), CIMNE (*htpp://www.gidhome.com*).

[41] Hill, R., The Mathematical Theory of Plasticity, Oxford University Press (1950).

[42] Hughes,T.J.R., Equivalence of finite elements for nearly incompressible elasticity, Trans. ASME, J. Appl. Mech. (1977),44 (1): 181–183.

[43] Hughes, T.J.R. The Finite Element Method: Linear Static and Dynamic Finite Element Analysis, Prentice-Hall, Englewood Cliffs, New Jersey, 1987.

[44] Hughes, T.J.R. and Franca, L.P., A new finite element formulation for computational fluid dynamics: VII. The Stokes problem with various well-posed boundary conditions: Symmetric formulations that converge for all velocity/pressure spaces, Comput. Methods Appl. Mech. Engrg. (1987), 65 (1): 85–96.

[45] Hughes, T.J.R. , Generalization of selective integration procedure to anisotropic and nonlinear media, Internat. J. Numer. Methods Engrg. (1980), 15 (1): 1413–1418.

[46] Hughes, T.J.R., Franca, L. P., Balestra, M., A new finite element formulation for computational fluid dynamics: V. Circumventing the Babuška-Brezzi condition: A stable Petrov–Galerkin formulation of the Stokes problem accommodating equal-order interpolations, Comput. Methods Appl. Mech. Engrg. (1986), 59(1): 85–99.

[47] Krischok, A. and Linder, C., On the enhancement of low-order mixed finite element methods for the large deformation analysis of diffusion in solids, Internat. J. Numer. Methods Engrg. (2016), 106 (4): 278–297.

[48] Lafontaine, N., Rossi, R., Cervera M. and Chiumenti, M., Explicit mixed strain-displacement finite element for dynamic geometrically non-linear solid mechanics, Computational Mechanics (2015), 55: 543-559.

[49] Lafontaine, N., Rossi, R., Cervera M. and Chiumenti, Formulación mixta estabilizada explícita de elementos finitos para sólidos compresibles y quasi-incompresibles, Revista Internacional de Métodos Numéricos para Cálculo y Diseño en Ingeniería (2015), 169.

[50] Liu, J. and Marsden, A.L., A unified continuum and variational multiscale formulation for fluids, solids, and fluid–structure interaction, Computer Methods in Applied Mechanics and Engineering, (2018), 337:549-597.

[51] Malkus, D.S. Hughes, T.J.R. , Mixed finite element methods - Reduced and selective integration techniques: A unification of concepts, Comput. Methods Appl. Mech. Engrg. (1978), 15 (1): 68–81.

[52] Moreno, E., Larese, A. and Cervera, M., Modeling of Bingham and Herschel-Bulkley flows with mixed stabilized P1/P1 finite elements using orthogonal subgrid scales, Journal of Non-Newtonian Fluid Mechanics (2016), 228: 1-16, http://dx.doi.org/10.1016/j.jnnfm.2015.12.005.

[53] Maniatty, A. M., Liu, Y., Klaas, O. and Shephard, M.S., Stabilized finite element method for viscoplastic flow: formulation and a simple progressive solution strategy, Comput. Methods Appl. Mech. Engrg. (2001), 190(35–36): 4609–4625.

[54] Maniatty, A. M., Liu, Y., Klaas, O. and Shephard, M.S., , Higher order stabilized finite element method for hyperelastic finite deformation, Comput. Methods Appl. Mech. Engrg. (2002), 191(13–14): 1491–1503.

[55] Maniatty, A. M. and Liu, Y., Stabilized finite element method for viscoplastic flow: formulation with state variable evolution, Internat. J. Numer. Methods Engrg. (2003), 56 (2): 185–209.

[56] Masud, A. and Truster, T.J., A framework for residual-based stabilization of incompressible finite elasticity: Stabilized formulations and methods for linear triangles and tetrahedra, Comput. Methods Appl. Mech. Engrg., (2013) 267: 359–399.

[57] Nagtegaal, J.C., Park, D.M. and Rice, J.R., On numerically accurate finite element solutions in the fully plastic range, Comput. Methods Appl. Mech. Engrg. (1974), 4: 53–177.

[58] Onishi,Y., Iida, R., Amaya and K., F-bar aided edge-based smoothed finite element method using tetrahedral elements for finite deformation analysis of nearly incompressible solids, Internat. J. Numer. Methods Engrg. (2017),109 (11): 1582–1606.

[59] Papanastasiou, T. C., Flows of materials with yield. Journal of Rheology (1987), 31: 385–404.

[60] Puso, M.A. and Solberg, J., A stabilized nodally integrated tetrahedral, Internat. J. Numer. Methods Engrg. (2006), 67(6): 841–867.

[61] Rossi, S., Abboud, N. and Scovazzi, G., Implicit finite incompressible elastodynamics with linear finite elements: A stabilized method in rate form, Comput. Methods Appl. Mech. Engrg. (2016), 311: 208–249.

[62] Schröder, J, Wriggers, P., and Balzania, D., A new mixed finite element based on different approximations of the minors of deformation tensors, Computer Methods in Applied Mechanics and Engineering, (2011), 200:49–52

[63] Scovazzi, G., Carnes, B., Zeng, X. and Rossi, S., A simple, stable, and accurate linear tetrahedral finite element for transient, nearly, and fully incompressible solid dynamics: a dynamic variational multiscale approach, Int. J. Numer. Meth. Engng (2016), 106:799–839.

[64] Scovazzia, G., Song, T. and Zeng, X. , A velocity/stress mixed stabilized nodal finite element for elastodynamics: Analysis and computations with strongly and weakly enforced boundary conditions, Comput. Methods Appl. Mech. Engrg., (2017), 325: 532–576.

[65] Simo, J.C., Hughes, T.J.R., Computational Inelasticity, Springer-Verlag New York (1998), ISBN: 978-0-387-97520-7.

[66] Simo, J.C., Rifai, M.S., A class of mixed assumed strain methods and the method of incompatible modes, Internat. J. Numer. Methods Engrg. (1990), 29 (8): 1595–1638.

[67] R.I. Tanner, J.F. Milthorpe, Numerical simulation of the flow of fluids with yield stresses, Proceedings of the Third International Conference on Numerical Methods in Laminar and Turbulent Flow, Eds: C. Taylor, J.A. Johnson, W.R. Smith, Swansea, UK (1983), 680–690

[68] de Vivo, L., Marotti de Sciarra F., The B-bar method and the limitation principles, International Journal of Solids and Structures, (1999), 36(34): 5177-5206

[69] Zeng, X., Scovazzi, G., Abboud, N., Colomés O., Rossi, S., A dynamic variational multiscale method for viscoelasticity using linear tetrahedral elements, Int J Numer Meth Engng. (2017),112: 1951–2003.